Biomass and Bioenergy 215 (2026) 109626

Contents lists available at ScienceDirect

Biomass and Bioenergy

journal homepage: www.elsevier.com/locate/biombioe

A next-gen renewable biogas-fueled multi-product system; ML (ANFIS) decision-making and techno-environmental-economic/LCA optimization by ARO/PSO/GWO/NSGA-II metaheuristic algorithms

Zhao Shuqi [a], Yan Limei [a,*], Mohammad Nadeem Khan [b,**], Hyder H. Abed Balla [c,***], Mohana Alanazi [d], Umid Turdialiyev [e], Hind Albalawi [f], Yasser Fouad [g,****], Ibrahim Mahariq [h,i,j,*****]

[a] Key Laboratory for Enhanced Oil & Gas Recovery of the Ministry of Education, Northeast Petroleum University, Daqing, Heilongjiang, 163318, China
[b] Department of Mechanical and Industrial Engineering, College of Engineering, Majmaah University, Al-Majmaah, 11952, Saudi Arabia
[c] Aeronautical Technical department, Najaf Technical Institute, Al Furat Al Awsat Technical University, Najaf, Kufa, Iraq
[d] Department of Electrical Engineering, College of Engineering, Jouf University, Sakaka, 72388, Saudi Arabia
[e] Doctor of Technical Sciences, Department of Organic Chemistry, Andijan State Technical Institute, Bobur Avenue, 56. Andijan, Rector, Uzbekistan
[f] Department of Physics, College of Sciences, Princess Nourah bint Abdulrahman University, P.O. Box 84428, Riyadh, 11671, Saudi Arabia
[g] Department of Applied Mechanical Engineering, College of Applied Engineering, Muzahimiyah Branch, King Saud University, P.O. Box 800, Riyadh, 11421, Saudi Arabia
[h] Department of Electrical and Electronic Engineering, Faculty of Engineering and Architecture, Istanbul Gelisim University, Avcılar- Istanbul, Istanbul, 34310, Türkiye
[i] Department of Medical Research, China Medical University Hospital, China Medical University, Taichung, Taiwan
[j] University College, Korea University, Seoul, 02481, South Korea

ARTICLE INFO

Keywords:
Biogas-fueled combined power plant
Renewable energy
Air Brayton cycle
Kalina cycle
Life cycle assessment
Multi-objective optimization

ABSTRACT

The growing request for multi-product and sustainable energy systems has highlighted the requirement for the effective use of renewable energy sources, such as biogas, in combined power plants (CPPs). The performance and sustainability of CPPs are limited by traditional power-generation techniques, which frequently concentrate on individual outputs or disregard the integration of thermo-enviro-economic goals. This study suggests a revolutionary biogas-fueled CPP that combines open and closed air Brayton cycles with a modified Kalina cycle, serving the purpose of waste heat recovery and thermal integration, to simultaneously provide power, cool, and heat. Having modeled and analyzed the proposed trigeneration setup, backed by life cycle assessment, an Adaptive Neuro-Fuzzy Inference System was used to support system performance prediction. A multi-objective optimization (MOO) using four metaheuristic algorithms was used to obtain the optimum operating conditions, and sensitivity analysis was used to measure the effect of the design variables. The total exergy destruction for the baseline condition was 5036 kW and the total energy and exergy efficiencies were 59.86% and 36.51%, correspondingly. Economic analysis showed a 16.67-year payback period and an energy cost of 0.1796 \$/kWh. While retaining high efficiency (≈38.68%), four-objective optimization decreased economic and environmental effect (TPC ≈ 68 \$/GJ, COE ≈ 0.138 \$/kWh, SCE ≈ 0.206 kg/kWh). The findings show the potential of the CPP as a sustainable multi-product energy solution and provide practical tips for heat recovery, turbine optimization, and biogas management in real-world scenarios.

* Corresponding authors.
** Corresponding authors.
*** Corresponding authors.
**** Corresponding author.
***** Corresponding author. College of Engineering and Architecture, Gulf University for Science and Technology, Mishref, Kuwait.
E-mail addresses: 565735794@qq.com (Y. Limei), mn.khan@mu.edu.sa (M.N. Khan), hyderballa@atu.edu.iq (H.H. Abed Balla), yfouad@ksu.edu.sa (Y. Fouad), lbmmahariq@gmail.com (I. Mahariq).

https://doi.org/10.1016/j.biombioe.2026.109626
Received 25 March 2026; Received in revised form 25 May 2026; Accepted 25 May 2026
Available online 29 May 2026
0961-9534/

Nomenclature

Symbol	Description (units)
ANFIS	Adaptive Neuro-Fuzzy Inference System
ARO	Artificial Rabbits Optimization
CBC	Closed Brayton Cycle
COE	Cost Of Eenergy ($/kWh)
CO_2	Carbon dioxide
CPP	Combined Power Plant
E−100, E−101, E−102, …	Heat exchangers
EDEI	Environmental Damage Effective Index
EEI	Exergo-Environmental Index
EII	Exergo-environmental Impact Improvement
ESF	Exergetic Stability Factor
ESI	Exergetic Sustainability Index
$\dot{E}x_D$	Exergy destruction
$\dot{E}x_F$	Fuel exergy
$\dot{E}x_P$	Product exergy
GWO	Grey Wolf Optimizer
GWP	Global Warming Potential ($kgCO_2$-eq/h)
IRR	Internal Rate of Return
K-100, K-101	Compressors
LCA	Life Cycle Assessment
ML	Machine Learning
MAPE	Mean Absolute Percentage Error
MAE	Mean Absolute Error
MKC	Modified Kalina Cycle
MOO	Multi-Objective Optimization
$\dot{m}_{biogas}$	Biogas flow rate (kg/s)
NPV	Net present value (M$)
NSGA-II	Non-dominated Sorting Genetic Algorithm II
OBC	Open Brayton Cycle
P	Pressure (kPa)
P_{in}	Inlet pressure (kPa)
P_{out}	Outlet pressure (kPa)
PP	Payback Period (years)
PSO	Particle Swarm Optimization
P-100	Pumps
R^2	Determination coefficient
RMSE	Root Mean Square Error
SCE	Specific CO_2 Emission (kg/kWh)
T	Temperature (°C)
T-100, T-101	Turbines
TPC	Cost of Total Product ($/GJ)
V-100, V-101	Vessels
VLV-100, VLV-101, …	Valves
β_i	Ratio of exergy destruction
ε_i	Exergy efficiency

1. Introduction

With the growth of global energy demand, and the demand to minimize environmental impacts, the search for sustainable and effective energy systems has increased [1,2]. A renewable fuel mostly made from organic waste, such as agricultural residues and landfill material, biogas has a lot of potential to generate electricity while also solving waste management issues and lowering greenhouse gas emissions [3,4]. Traditional gas turbine power generation cycles in general are of low efficiency due to waste heat recovery efficiency, and they are widely used, such as Brayton cycles. This restriction may be avoided if advanced thermodynamic cycles like Kalina cycle are added which use low quality heat sources to increase the efficiency of energy conversion [5,6].

An integrated combined power plant (CPP) has been developed in order to maximize the energy usage, minimize the environmental impact and financial costs. Traditional power systems are usually run independently and are only concerned with the production of electricity. The traditional one size fits all approach does not consider the benefits of simultaneous generation of both electricity and heat and cooling (cogeneration). The higher overall efficiencies, and sustainable energy practices, can be realized by the use of biogas as a source of fuel [7,8].

But many obstacles must be overcome to make these types of integrated systems common-place. These are the variable supply of biogas, complex system design, and a sophisticated system control to handle the interaction of multiple cycles, all of which may compromise the stability of the set-up. To overcome these setbacks, novel engineering solutions and global performance assessments are needed to provide reliability and viability of integrated CPPs [8,9].

1.1. Related research

A variety of configurations of biogas-based power systems have been studied in recent times. A multi-generation framework using a biogas-assisted Brayton cycle to generate electricity, heat and cool was proposed by Zuo et al. [10]. All of this was integrated into their design, a supercritical carbon dioxide (CO_2) cycle, humidification-dehumidification desalination, a steam methane reforming (SMR) gas turbine, and syngas–based methanol synthesis. The configuration involving thermodynamic, exergo-economic and environmental analysis indicated high efficiency and cost-effectiveness of the installation with 33.33 percent exergy efficiency, 13018 kW of electricity, 2.52 kg/s of drinking water, 0.491 kg/s of methanol and payback period of 2.79 years, using multi-objective optimization (MOO). Similar to this, Firouzy et al. [11] created a biogas-fired SMR system for waste heat recovery that was connected to a supercritical CO_2 Brayton cycle. This system produced 1.35 ton/hr and had remarkable energy and exergy efficiencies of 84.96% and 59.89%, respectively. Thermodynamic analysis identified the combustion chamber as the major source of exergy destruction (over 64%), while parametric studies showed that increasing the steam-to-carbon ratio and reforming temperature enhances hydrogen output but reduces net power. Thus, the findings demonstrated the setup's ability for efficient, sustainable poly-generation using biogas. With an emphasis on thermodynamic, exergo-economic, and MOO analyses, Sadri Irani and Fattahi [12] investigated a combined Brayton-Kalina cycle with proton exchange membrane (PEM) hydrogen production unit. Results showed that the Brayton cycle accounted for the highest exergy destruction (58%) and investment cost, followed by the Kalina cycle (40%), while the PEM unit required only ~1% of costs. Optimization using non-dominated sorting genetic algorithm II (NSGA-II) improved total energy and exergy efficiencies by 6% and 3%, respectively, though with a 15% increase in investment cost. For waste heat recovery from a naval low-speed diesel engine, Feng et al. [6] suggested a combined supercritical CO_2 Brayton-Kalina cycle. By efficiently using exhaust and bypass heat to generate electricity, the system reduced annual fuel consumption by 16.62% and the ship's energy efficiency design index by 15.01%, according to thermodynamic and optimization calculations. Moreover, for providing decarbonized power, Ahmad and Aziz [13] presented an integrated system that combines chemical looping hydrogen generation, ammonia synthesis, and an existing natural gas combined cycle (NGCC). External heat and dividing oxygen carriers were the two systems that were examined; the latter had cheaper levelized cost (0.108 USD/kWh) and greater efficiency (47.1% energy, 41.6% exergy). In addition to reducing CO_2 emissions while preserving NGCC-equivalent NOx levels, the system allows H_2–NH_3 co-firing and exhibits the potential for negative emissions through CO_2 sequestration.

Therefore, these investigations have proven the possibility of using more complicated thermodynamic cycles to improve the efficiency of biogas-based power systems. Nevertheless, to provide a comprehensive evaluation of system performance, thorough analyses that take into account energy and exergy efficiencies as well as economic and environmental effects are still required.

Moreover, sophisticated modelling tools have recently emerged as a key enabler for optimizing complex thermal energy systems. For instance, Shuqi et al. [14] achieved a 46% performance enhancement in microchannel heat sinks by identifying optimal geometric baffle parameters through accurate artificial neural network (ANN)-based predictive modeling. For enhancing the operational efficiency of integrated power and heating setups, Wan et al. [15] introduced a sophisticated closed-loop framework integrating Temporal Convolutional Networks, attention mechanisms, and reinforcement learning, which demonstrated superior accuracy in multi-unit load allocation and significant reductions in carbon emissions. Cheng et al. [16] showcased the potential

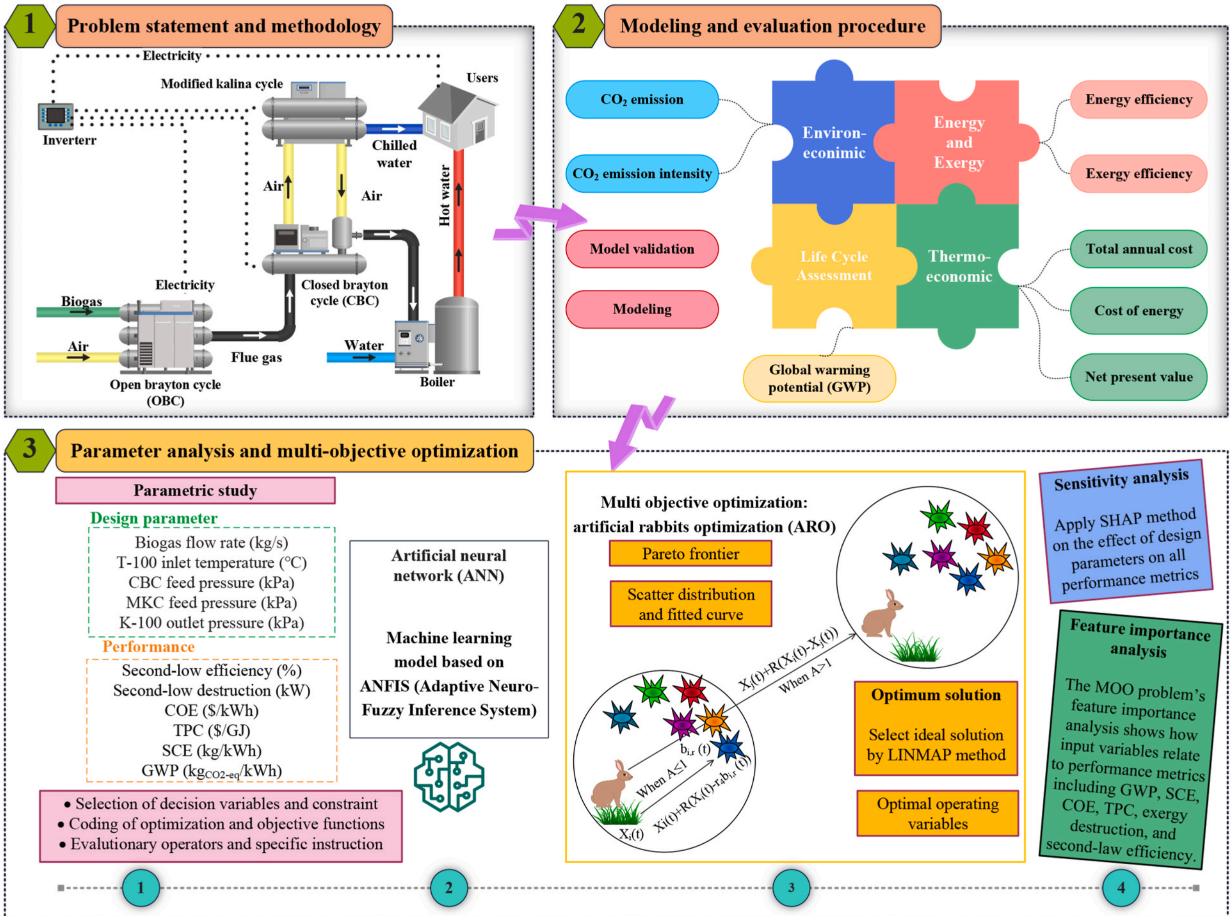

Fig. 1. Modeling flowchart of the newly presented biogas-fired CPP.

of multi-layer perceptron (MLP) models in uncovering critical geometric dependencies to achieve massive performance gains in fluid-flow components. Together, these studies underscore how sophisticated predictive and prescriptive models are taking the place of conventional numerical methods in engineering design and operational efficiency.

1.2. Gaps, novelty, and contributions

Although the technology for biogas power generation has progressed a long way, there are still many questions left unanswered. Most past research has dealt with a single discrete element such as thermodynamic efficiency or economic performance, and not provided an integrated model that addresses energy, exergy, environmental and economic considerations. In addition, there is inadequate research on the control of entropy generation and exergy destruction by system configurations. The impact of crucial operating parameters, especially turbine inlet temperature, on the overall sustainability and performance of such systems is another neglected area. Furthermore, not much work has been done to use sophisticated computational techniques like machine learning (ML) to forecast system behavior and assist in performance optimization in a variety of scenarios [17,18].

In the present research, a modified Kalina cycle fueled by biogas is combined with an open-closed air Brayton cycle to create a novel CPP structure. Thus, the integration of an open-closed air Brayton cycle with a modified biogas-fueled Kalina cycle is what makes this study novel and includes multiple significant contributions. By using air as the working fluid, both open and closed Brayton cycles is used simultaneously to increase efficiency and lessen their negative effects on the environment. The modified Kalina cycle efficiently uses the waste heat from the closed Brayton cycle through thermal coupling to produce more electricity and cooling. A comprehensive thermo-enviro-economic report, supported by a life cycle assessment (LCA), provides the global performance of the entire system in terms of implementation. Parametric study underlines further the sustainability of energy generation potential of the system, as optimization of design variables is fundamental to higher efficiency and reduced exergy destruction, economic and environmental effects. Also, a complex ML model is utilized to predict meaningful parameters of the system, developing a better concept of the working and making effective decisions. Additionally, MOO methods are also used to create a balance between efficiency, cost, and environmental impact to achieve the optimal system design. Finally, a sensitivity analysis based on SHAP is also included in order to quantify the relative importance of the key decision variables and thus understand the relationships between variables and their effects on the efficiency, economic, and environmental outcomes.

Overall, this combined strategy, being able to minimize CO_2 emissions, raise efficiency of resources, and promote the adoption of renewable biogas-based systems, does not only maximize the use of energy but also facilitates sustainable and financially viable energy culture.

2. Methodology

Fig. 1 shows the overall modeling framework of the present project. The methodological framework for the current study is organized into three main integrated stages for assessing and optimizing the proposed biogas-fired CPP. First, the thermodynamic model is defined by integrating the open Brayton cycle, the modified Kalina cycle, and the closed Brayton cycle, where mass and energy balance equations—constrained by the system's operational boundaries—establish the core simulation

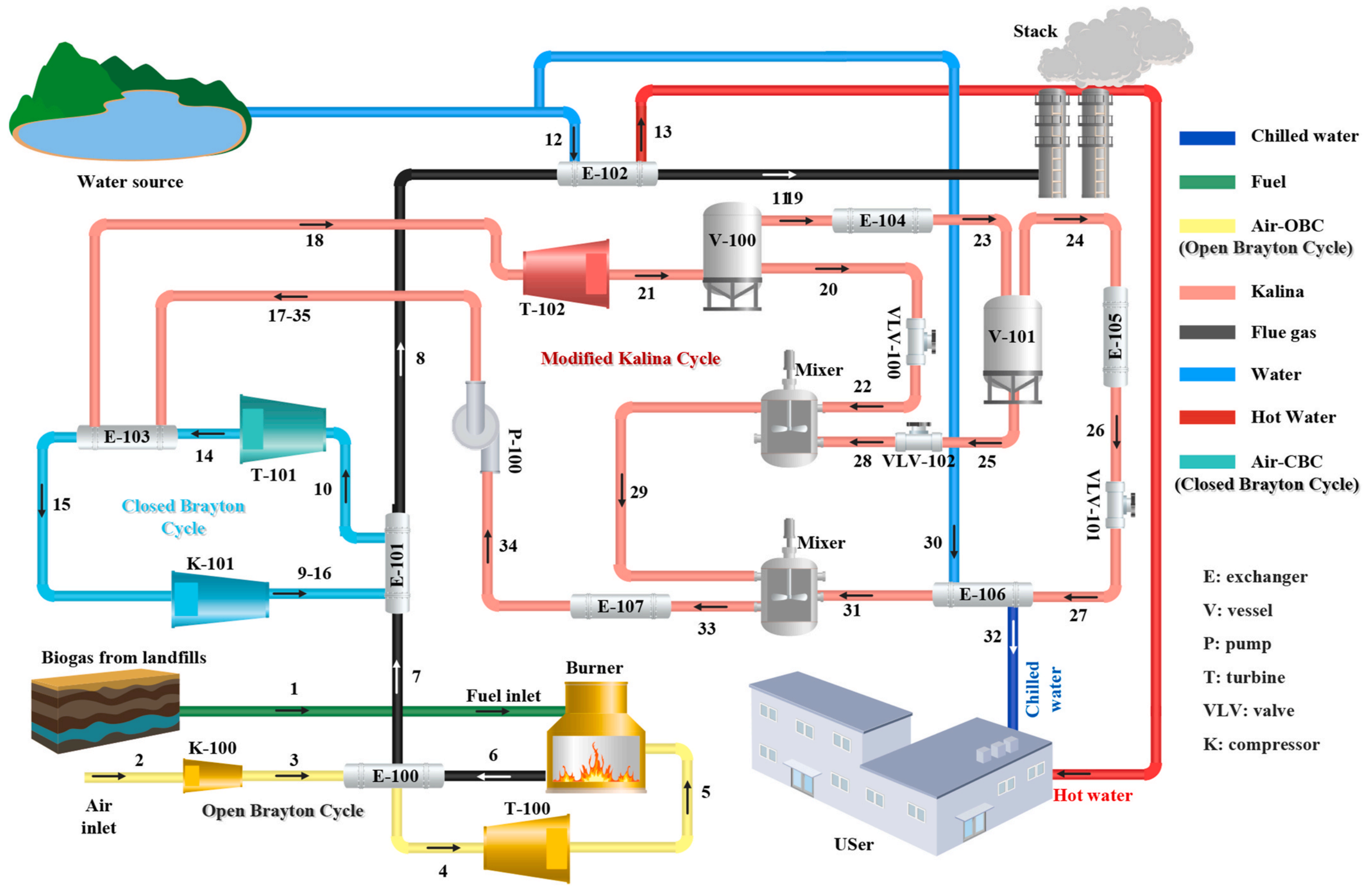

Fig. 2. Process flow diagram of the newly studied biogas-fueled CPP employing open-closed air Brayton cycle configuration.

environment. Second, the performance is evaluated through a comprehensive multi-criteria approach, incorporating energy-exergy analysis, thermo-economic assessment, and environmental investigation, all of which are validated against established literature to ensure model accuracy. Finally, a parametric study is conducted to identify key design variables, followed by the deployment of an ML-based surrogate model (employing ANFIS) to facilitate MOO applying the Artificial Rabbits Optimization (ARO) algorithm. To ensure robust decision-making and interpretability, the Pareto frontiers are analyzed using the LINMAP method [19], and SHAP-based sensitivity and feature-importance analyses are applied to rigorously quantify the influence of design parameters on thermo-enviro-economic system-performance metrics.

2.1. Characterization of the CPP

The integrated biogas-fueled energy plant presented in this study can generate electricity, chilled water and hot water. The proposed setup is innovative by two important features; i.e.

1. Increased waste heat recovery by thermal linking of an optimized Kalina cycle with a closed Brayton cycle.
2. Applying both dual (closed and open) Brayton cycles, with air as the working fluid.

The open Brayton cycle utilizes a gas turbine for producing electricity by burning biogas from landfills with air. The closed Brayton cycle is then powered by the hot flue gases, and any remaining energy is recovered in a boiler to provide hot water. The waste heat from the closed Brayton cycle is moved to the modified Kalina subsystem in order to maximize energy use and further increase system efficiency. This cycle efficiently eliminates the requirement for a separate refrigeration cycle by generating cooling energy through an enrichment–evaporation process and extra electricity through an expansion turbine.

The proposed CPP will bring a number of benefits.

- Less dependence on fossil fuels by using renewable biogas
- Ability to provide several products (electricity, heat, cooling) to industry and households
- Mitigation of methane and CO_2 emissions through biogas utilization.

But there are some plant-specific issues to consider.

- Advanced control strategies are needed to achieve a high level of thermal integration and maintain stable operation in dynamic conditions.
- Continuous and reliable biogas supply is essential to maintain system performance.

Generally, the plant is more energy efficient than conventional single-purpose facilities as it creates three valuable products – electricity, cooling, and heating. Entropy formation is declined and total energy efficiency is raised by utilizing waste heat at several stages. The boiler is used to provide heating and the Kalina subsystem is used to provide cooling. It generates electricity from three major subsystems; open Brayton cycle, closed Brayton cycle and enhanced Kalina cycle. Most importantly, due to its ease of availability, lack of toxicity and operational experience, air is employed as the working fluid in both Brayton cycles.

The process flow diagram of the studied CPP, which is intended to produce electricity, cold water, and hot water all at once, is illustrated in Fig. 2. The combustion air (stream 2) is compressed in a compressor K-100 and subsequently is heated in a heat exchanger. After expanding via

Table 1
Input equipment data specifications for the newly proposed biogas-powered CPP [26–29].

Power	Value
Fuel rate (kg/s)	1.0
Air to burner (kg/s)	3.77
K-100 outlet pressure (kPa)	800
Stream 4 temperature (°C)	1200
T-100 outlet pressure (kPa)	101.3
T-101 outlet pressure (kPa)	101.3
T-101 inlet pressure (kPa)	900
K-101 outlet pressure (kPa)	900
Stream 15 temperature (°C)	40
Stream 10 temperature (°C)	600
T-102 outlet pressure (kPa)	1050
T-102 inlet pressure (kPa)	4000
Stream 23 temperature (°C)	90
Stream 26 temperature (°C)	26
Stream 31 temperature (°C)	12
VLV-101 outlet pressure (kPa)	355
Hot water temperature (°C)	80
Chilled water temperature (°C)	9
Dead state pressure (kPa)	101.3
Dead state temperature (°C)	25
Biogas composition (%)	35% methane (CH_4), 50% CO_2, 15% N_2
Turbine isentropic efficiency (%)	90
Compressor isentropic efficiency (%)	90
Pump adiabatic efficiency (%)	75

turbine T-100, the compressed air enters the burner and is combined with biogas fuel (stream 1). The energy released by the fuel's combustion is transmitted through the flue gas (stream 6) and two heat exchangers, E−100 and E−101, where it warms the working fluid in the closed Brayton cycle.

Significant thermal energy is still present in the flue gas after E−101, and this energy is used in the boiler E−102 to produce a hot water stream. Compressed air leaving compressor K-101 (stream 10) is heated in E−101 before expanding in turbine T-101 to generate electricity within the closed Brayton cycle. The high-temperature hot air from the T-101 enters E−103 and then the vapor generator of the modified Kalina cycle. This step not only gives heat to Kalina cycle, but also decreases the air temperature in K-101 before it is recompressed.

The working fluid of the Kalina cycle is water-ammonia. In E−103, the fluid absorbs heat at high pressure, which causes vaporization. Additional power is produced as the vapor expands through turbine T-102. The two-phase mixture that results from expansion-induced partial condensation is separated in vessel V-100. While the liquid fraction is sent to the mixer after going through the expansion valve VLV-100, the vapor fraction (stream 19) is partially condensed in E−104. The liquid fraction is sent to the mixer via expansion valve VLV-102, while the outlet stream from E−104 goes through additional phase separation in V-101, creating an ammonia-rich vapor (stream 24) that condenses in E−105.

Through the Joule-Thomson valve VLV-101, the condensed refrigerant from E−105 is expanded and sent to the low-temperature evaporator E−106, which produces chilled water (stream 32). After passing through the evaporator, the refrigerant enters the mixer and mixes with the other liquid streams. The cycle is completed when the final mixture is recycled to E−103 after being fully condensed in E−107 and pressurized by pump P-100.

2.2. Simulation of the CPP

The Aspen HYSYS simulation platform was used to model the proposed biogas-powered CPP, encompassing the water boiler, modified Kalina, open Brayton, and closed Brayton cycles. The Peng-Robinson equation of state (EOS) was selected as the thermodynamic property package to ensure accurate phase behavior and energy balance calculations, as it is well-validated for hydrocarbon-based power systems and complex petrochemical cycles [20–24]. The combustion chamber model used was a Gibbs reactor model, which is used to find the equilibrium composition of the products by minimizing the total Gibbs free energy of the system [25]. This approach allows for the simulation of conversion without requiring predefined stoichiometric reaction pathways.

The combustion air and biogas feed stream was calculated in Aspen HYSYS when inlet conditions (temperature, pressure, flow rate and composition) were provided [26]. Following that, equipment data was added to the simulation in accordance with the specifications compiled in Table 1, guaranteeing that each unit operation was correctly defined and arranged in a sequential manner. The flowsheet was able to converge, balancing the degrees of freedom, so the software could solve the coupled mass and energy equations. Also, the simulation results were checked and validated with the result available in the literature for the development of the model to check the accuracy of the developed model.

The basic assumptions used in the simulation are also listed as follows.

- The system operates under steady-state conditions [30].
- The efficiencies of turbines, pumps, and compressors are fixed at 0.85 [30].
- Heat losses to the surroundings are considered negligible [31].
- The working fluid of the Kalina cycle is a water-ammonia mixture [32].
- The enthalpy of inlet and outlet streams across the expansion valves is assumed equal [33].
- Potential and kinetic exergy variations are neglected [34].

2.3. Process analysis of the CPP

2.3.1. Energy-exergy performance analysis approach

First-law (energy) investigation measures quantity of energy in a system and determines how efficient each part and the plant as a whole are. This method is constrained, though, as it solely takes into account the amount of energy, ignoring the quality of energy flows or the maximum amount of useful work that can be extracted. To overcome this limitation a second-law (exergy) analysis is employed to consider energy quality and to highlight areas for improvement [35].

The fundamental energy balance for any system component is expressed as [36]:

$$\dot{Q} - \dot{W} = \sum (\dot{m}h)_i - \sum (\dot{m}h)_o \tag{1}$$

where $\dot{W}$ and $\dot{Q}$ represent the power and heat rates, respectively, h is the specific enthalpy, $\dot{m}$ is the mass flow rate, and the subscripts i and o denote inlet and outlet streams.

By taking into consideration the useful work potential of energy streams, exergy analysis broadens this viewpoint. The sum of the physical, chemical, kinetic, and potential exergies is the total exergy of the j-th stream [37]:

$$ex_j = ex_j^{ph} + ex_j^{ch} + ex_j^{kn} + ex_j^{pt} \tag{2}$$

Only physical and chemical exergy were taken into consideration in this study because kinetic and potential contributions were disregarded [38]. They are stated as [37,39,40]:

$$ex_j^{ph} = (h_j - h_0) - T_0 \times (s_j - s_0) \tag{3}$$

$$ex_j^{ch} = \sum x_j ex_j^0 + G - \sum x_j G_j \tag{4}$$

Here, s_0 and h_0 are the entropy and enthalpy at reference conditions (ambient temperature and pressure), s_j and h_j are the values at operating conditions, x_j is the mole fraction, ex_j^0 is the standard chemical exergy, and G and G_j represent the Gibbs free energy of the mixture and

Table 2
Energy balance and exergy destruction equations for individual component of the newly proposed CPP process.

Components	Energy	Exergy
K-100	$\dot{m}_2h_2 + \dot{W} = \dot{m}_3h_3$	$\dot{E}_2 + \dot{W} - \dot{E}_3$
K-101	$\dot{m}_{15}h_{15} + \dot{W} = \dot{m}_{16}h_{16}$	$\dot{E}_{15} + \dot{W} - \dot{E}_{16}$
E−100	$\dot{m}_3h_3 + \dot{m}_6h_6 = \dot{m}_4h_4 + \dot{m}_7h_7$	$\dot{E}_3 + \dot{E}_6 - \dot{E}_4 - \dot{E}_7$
E−101	$\dot{m}_7h_7 + \dot{m}_9h_9 = \dot{m}_8h_8 + \dot{m}_{10}h_{10}$	$\dot{E}_7 + \dot{E}_9 - \dot{E}_8 - \dot{E}_{10}$
E−102	$\dot{m}_{12}h_{12} + \dot{m}_8h_8 = \dot{m}_{11}h_{11} + \dot{m}_{13}h_{13}$	$\dot{E}_{12} + \dot{E}_8 - \dot{E}_{11} - \dot{E}_{13}$
E−103	$\dot{m}_{14}h_{14} + \dot{m}_{17}h_{17} = \dot{m}_{15}h_{15} + \dot{m}_{18}h_{18}$	$\dot{E}_{14} + \dot{E}_{17} - \dot{E}_{15} - \dot{E}_{18}$
E−104	$\dot{m}_{19}h_{19} = \dot{Q} + \dot{m}_{23}h_{23}$	$\dot{E}_{19} - \dot{E}_{23}$
E−105	$\dot{m}_{24}h_{24} = \dot{Q} + \dot{m}_{26}h_{26}$	$\dot{E}_{24} - \dot{E}_{26}$
E−106	$\dot{m}_{27}h_{27} + \dot{m}_{30}h_{30} = \dot{m}_{32}h_{32} + \dot{m}_{31}h_{31}$	$\dot{E}_{27} + \dot{E}_{30} - \dot{E}_{32} - \dot{E}_{31}$
E−107	$\dot{m}_{33}h_{33} = \dot{Q} + \dot{m}_{34}h_{34}$	$\dot{E}_{33} - \dot{E}_{34}$
T-100	$\dot{m}_4h_4 = \dot{W} + \dot{m}_5h_5$	$\dot{E}_4 - \dot{W} - \dot{E}_5$
T-101	$\dot{m}_{10}h_{10} = \dot{W} + \dot{m}_{14}h_{14}$	$\dot{E}_{10} - \dot{W} - \dot{E}_{14}$
T-102	$\dot{m}_{18}h_{18} = \dot{W} + \dot{m}_{21}h_{21}$	$\dot{E}_{18} - \dot{W} - \dot{E}_{21}$
V-100	$\dot{m}_{21}h_{21} = \dot{m}_{19}h_{19} + \dot{m}_{20}h_{20}$	$\dot{E}_{21} - \dot{E}_{19} - \dot{E}_{20}$
V-101	$\dot{m}_{23}h_{23} = \dot{m}_{24}h_{24} + \dot{m}_{25}h_{25}$	$\dot{E}_{23} - \dot{E}_{24} - \dot{E}_{25}$
VLV-100	$\dot{m}_{20}h_{20} = \dot{m}_{22}h_{22}$	$\dot{E}_{20} - \dot{E}_{22}$
VLV-101	$\dot{m}_{26}h_{26} = \dot{m}_{27}h_{27}$	$\dot{E}_{26} - \dot{E}_{27}$
VLV-102	$\dot{m}_{25}h_{25} = \dot{m}_{28}h_{28}$	$\dot{E}_{25} - \dot{E}_{28}$
Burner	$\dot{m}_1h_1 + \dot{m}_5h_5 = \dot{m}_6h_6$	$\dot{E}_1 + \dot{E}_5 - \dot{E}_6$

Table 3
Parameter values required for economic evaluation.

Parameters	Value	Ref.
Working hours (H)	8000 h	[52]
System life time (L)	25 years	[53]
Interest rate (I_r)	5 %	[54]
CEPCI for 2024	800.3	[13]
Cost of CO_2 ($C_{CO_{2,f}}$)	87 ($/ton)	[48]
Cost of biogas ($C_{bio,f}$)	2 ($/GJ)	[55]
Cost of power (C_{power})	0.3 ($/kWh)	[55]
Cost of heating ($C_{heating}$)	0.02 ($/kWh)	[56]
Cost of cooling ($C_{cooling}$)	0.08 ($/kWh)	[57]

Table 4
Cost functions utilized for estimating each equipment cost in the new CPP process.

Cost function	Component	Ref.	Base year	CEPCI (2024)
$6000 \times \dot{W}_T^{0.7}$	Turbine	[58]	2013	567
$3540 \times \dot{W}_p^{0.71}$	Pump	[59]	2011	586
$516.62 \times A^{0.6}$	Exchanger	[60]	2001	394
$\frac{46.08 \times \dot{m}_{in}}{0.995 - \frac{P_o}{P_i}} \times (1 + e^{0.018T_6 - 26.4})$	Combustion chamber	[48]	2001	394
$91562 \times \left(\frac{\dot{W}}{445}\right)^{0.6}$	Compressor	[61]	2003	402

Table 5
ANFIS model structure and hyperparameter settings.

Parameters	Value/Description
Fuzzy structure	Sugeno type
Initial FIS for training	Genfis2
Membership function type	Dsigmf
Cluster center range of influence	0.45
Number of input	5
Number of output	13
Number of fuzzy rules	10
Optimization method	Hybrid

component, respectively.

Table 6
System design parameter boundaries for the MOO study.

Design parameter	Lower bound	Upper bound
$\dot{m}_{biogas}$ (kg/s)	0.5	2.5
$T_{in\ T-100}$ (°C)	1200	1600
$P_{CBC\ feed}$ (kPa)	900	1200
$P_{MKC\ feed}$ (kPa)	2000	5000
$P_{out\ k-100}$ (kPa)	300	800

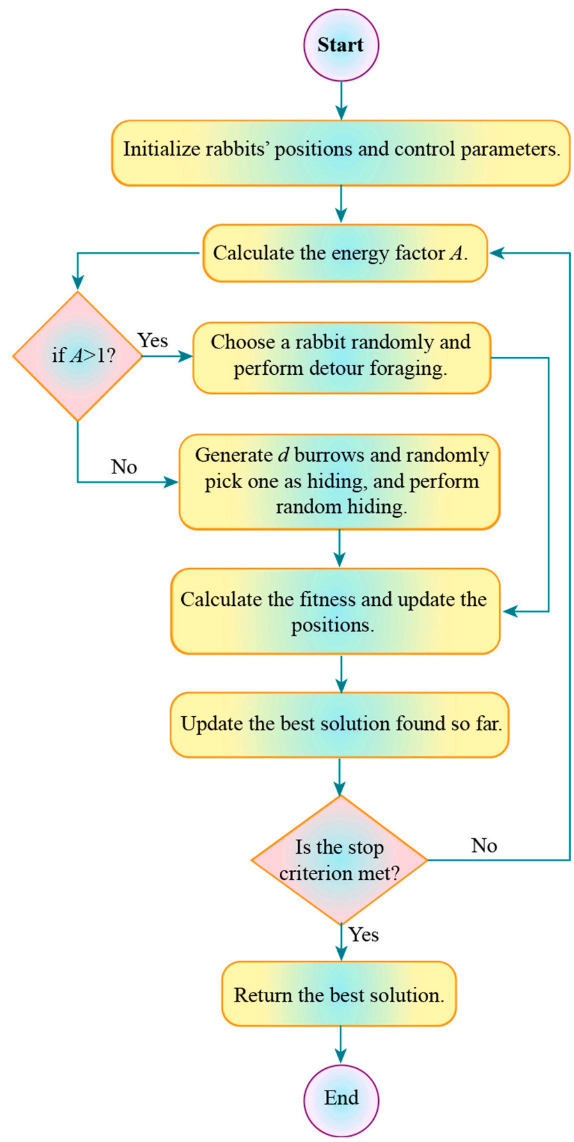

Fig. 3. Flowchart of the ARO algorithm workflow [70].

The exergy balance for each system component is determined as Eq. (5), in which $\dot{E}x_F$ is the fuel exergy input, $\dot{E}x_D$ the destroyed exergy, and $\dot{E}x_P$ is the useful product exergy [41,42].

$$\dot{E}x_F = \dot{E}x_D + \dot{E}x_P \tag{5}$$

Based on this balance, two key performance parameters are defined [41,43,44]:

$$\varepsilon_i = 1 - \frac{\dot{E}x_{D,i}}{\dot{E}x_{F,i}} \tag{6}$$

Table 7
Selected values for hyperparameters of each optimization algorithm.

Description	Value
PSO	
Particle number, Np	40
Maximum iteration	300
Archive number	20
Partition number	150
Weight factor	2.50
Learning parameters	0.90
Learning parameters	0.90
Total Function Evaluations	11000
Average Execution Time (s)	~135
GWO	
Maximum iteration	300
q initial	2.00
r_1 and r_2	0.5
Total Function Evaluations	8000
Average Execution Time (s)	~105
NSGA-II	
Population size	100
Number of generation	300
Crossover probability	0.85
Mutation probability	0.15
Total Function Evaluations	25000
Average Execution Time (s)	~290
ARO	
Particle number, Np	300
Depth factor	55
Multiplier weight	0.25
Total Function Evaluations	9000
Average Execution Time (s)	~110

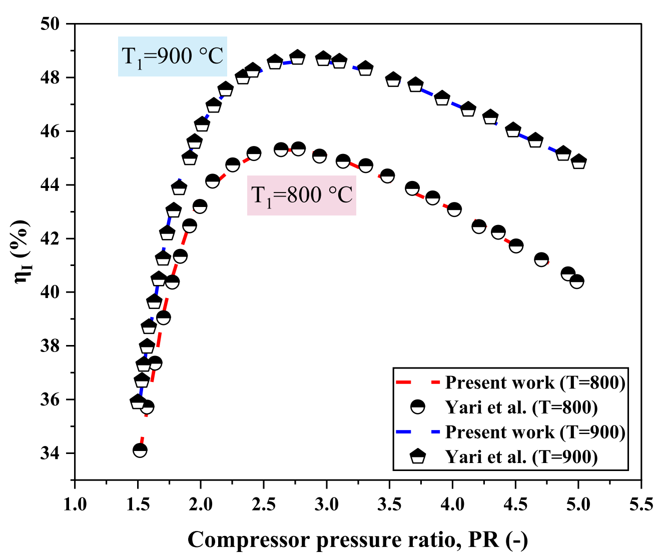

Fig. 4. Comparing OBC simulation results using biogas fuel between the present work and Ref. [74] at different turbine inlet temperatures.

$$\beta_i = \frac{\dot{E}x_{D,i}}{\sum \dot{E}x_{D,i}} \tag{7}$$

where ε_i presents the exergy efficiency and β_i the exergy destruction ratio for the i-th component. Table 2 presents the component-specific energy conservation and exergy destruction equations.

Additionally, the associated energy and exergy inputs are computed as follows since biogas serves as the system fuel [45]:

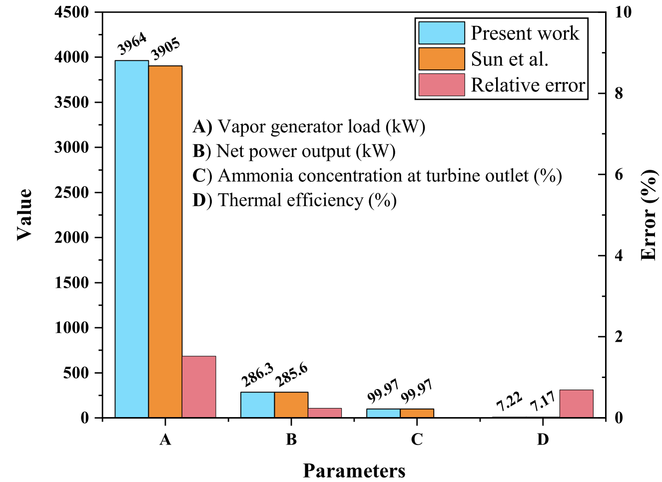

Fig. 5. Comparing MKC simulation results between the present work and Ref. [75].

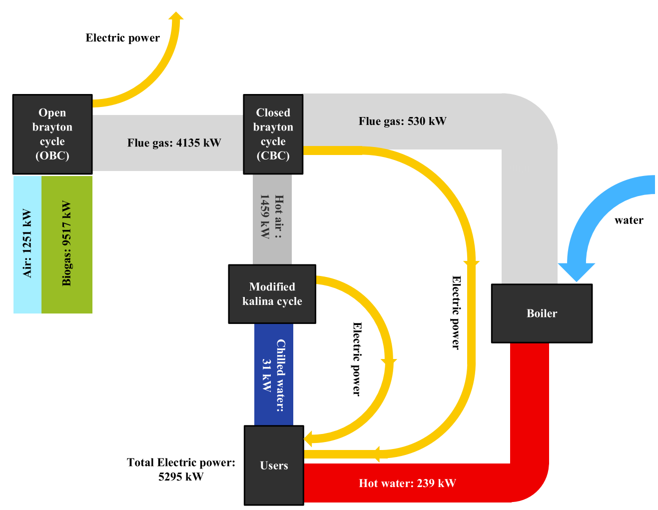

Fig. 6. Fuel and product exergy flow for the newly studied biogas-powered CPP.

Table 8
Results of exergy analysis estimations for the individual equipment utilized in the proposed CPP process.

Component	$\dot{E}x_F$	$\dot{E}x_P$	$\dot{E}x_D$	ε_i	β_i
K-100	1011	956	55	94.55	1.09
E−100	3327	2725	602	81.90	11.95
T-100	2431	2345	86	96.46	1.70
Burner	10768	8860	1908	82.28	37.88
E−101	4135	3446	689	83.33	13.68
T-101	7834	7352	482	93.84	9.57
K-101	5893	5595	298	94.94	5.91
E−102	530	129	401	24.33	7.96
E−103	1459	1316	143	90.19	2.83
T-102	459	423	36	92.15	0.71
V-100	931	931	0	99.99	0.00
VLV-100	16	14	2	87.50	0.03
E−104	913	695	218	76.12	4.32
V-101	217	217	0	9.99	0.00
VLV-102	42	37	5	88.09	0.09
E−105	176	155	21	88.06	0.416
VLV-101	144	140	4	97.22	0.07
E−106	52	15	37	28.84	0.73
E−107	117	70	47	59.82	0.93
P-100	12	10	2	83.33	0.03

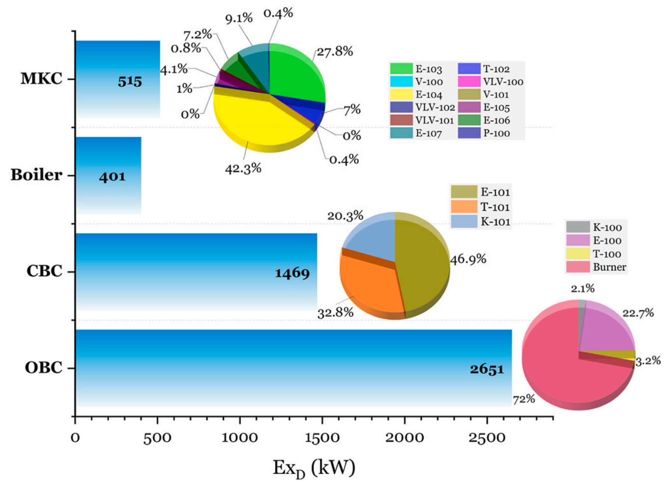

Fig. 7. Exergy destruction breakdown by the employed subsystems and their relevant components.

Table 9
Investment costs of individual CPP components adjusted for 2024 and corresponding cost rates.

Name	Equipment cost ($)	Equipment cost for 2024 ($)	Equipment cost rate ($/h)
K-101	19771500	39361024	418.49
P-100	71200	97238	1.03
E−106	24000	48749	0.52
E−105	23900	48546	0.52
Burner	136889	278051	2.96
E−100	36521	74182	0.79
T-102	313500	442494	4.70
E−102	53300	108264	1.15
E−101	56985	115749	1.23
E−104	17600	35749	0.38
E−103	914900	1858362	19.76
K-100	2847600	5668991	60.27
T-101	3052355	4308289	45.81
E−107	84200	171029	1.82
T-100	1371675	1936070	20.58

$$\dot{Q}_f = \dot{m}_f \times LHV_f \tag{8}$$

$$\dot{E}x_f = \dot{E}x_f^{ph} + \dot{E}x_f^{ch} \tag{9}$$

$$LHV_f = H_{prod} - H_{reactant} \tag{10}$$

Biogas combustion generates electricity in the open Brayton cycle (OBC), and this cycle energy efficiency is described as follows:

$$\eta_{OBC} = \frac{\dot{W}_{T100} - \dot{W}_{K100}}{\dot{Q}_f} \tag{11}$$

The energy efficiency for the closed Brayton cycle (CBC), in which power generation is driven by recovered heat, is stated as follows:

$$\eta_{CBC} = \frac{\dot{W}_{T101} - \dot{W}_{K101}}{\dot{m}_7(h_7 - h_8)} \tag{12}$$

In the boiler, the heating power ($\dot{Q}_h$) and exergy of the hot-water stream ($\dot{E}x_h$) are given by:

$$\dot{Q}_h = \dot{m}_8(h_8 - h_{11}) \tag{13}$$

$$\dot{E}x_h = \dot{Q}_h\left(1 - \frac{T_0}{T_H}\right) \tag{14}$$

CBC waste heat powers the modified Kalina cycle (MKC), which produces electricity and cooling. The energy efficiency of this device is:

$$\eta_{MKC} = \frac{\dot{W}_{T102} - \dot{W}_{P100} + \dot{Q}_c}{\dot{m}_{14}(h_{14} - h_{15})} \tag{15}$$

The cooling power ($\dot{Q}_c$) and cooling exergy ($\dot{E}x_c$) are defined as:

$$\dot{Q}_c = \dot{m}_{31}(h_{31} - h_{27}) \tag{16}$$

$$\dot{E}x_c = \dot{Q}_c\left(\frac{T_0}{T_C} - 1\right) \tag{17}$$

Accordingly, the overall efficiencies of the integrated CPP are determined as:

$$\eta_{sys} = \frac{\dot{W}_{net} + \dot{Q}_c + \dot{Q}_h}{\dot{Q}_f} \tag{18}$$

$$\varepsilon_{sys} = \frac{\dot{W}_{net} + \dot{E}x_c + \dot{E}x_h}{\dot{E}x_f} \tag{19}$$

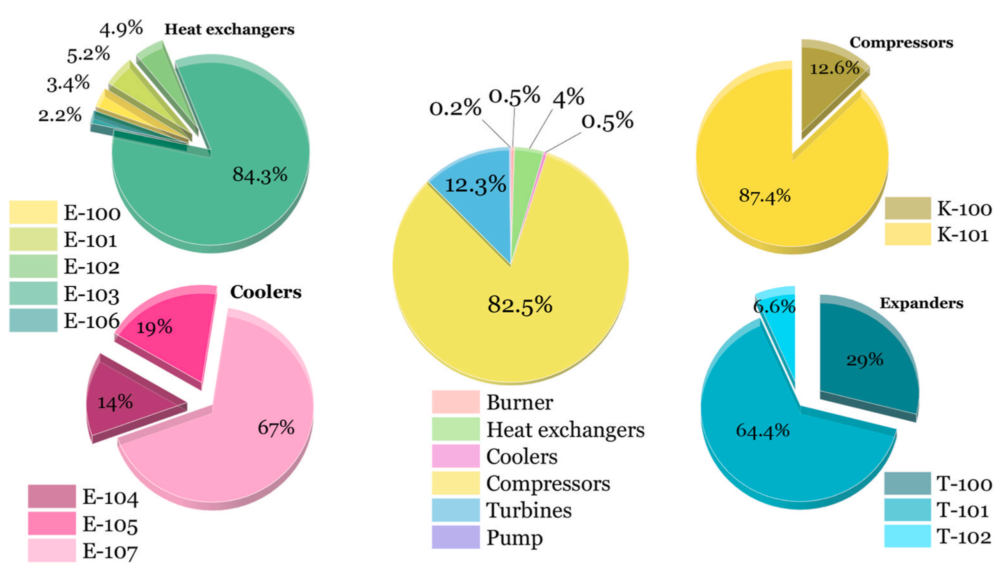

Fig. 8. Breakdown of investment costs for the key components in the proposed CPP.

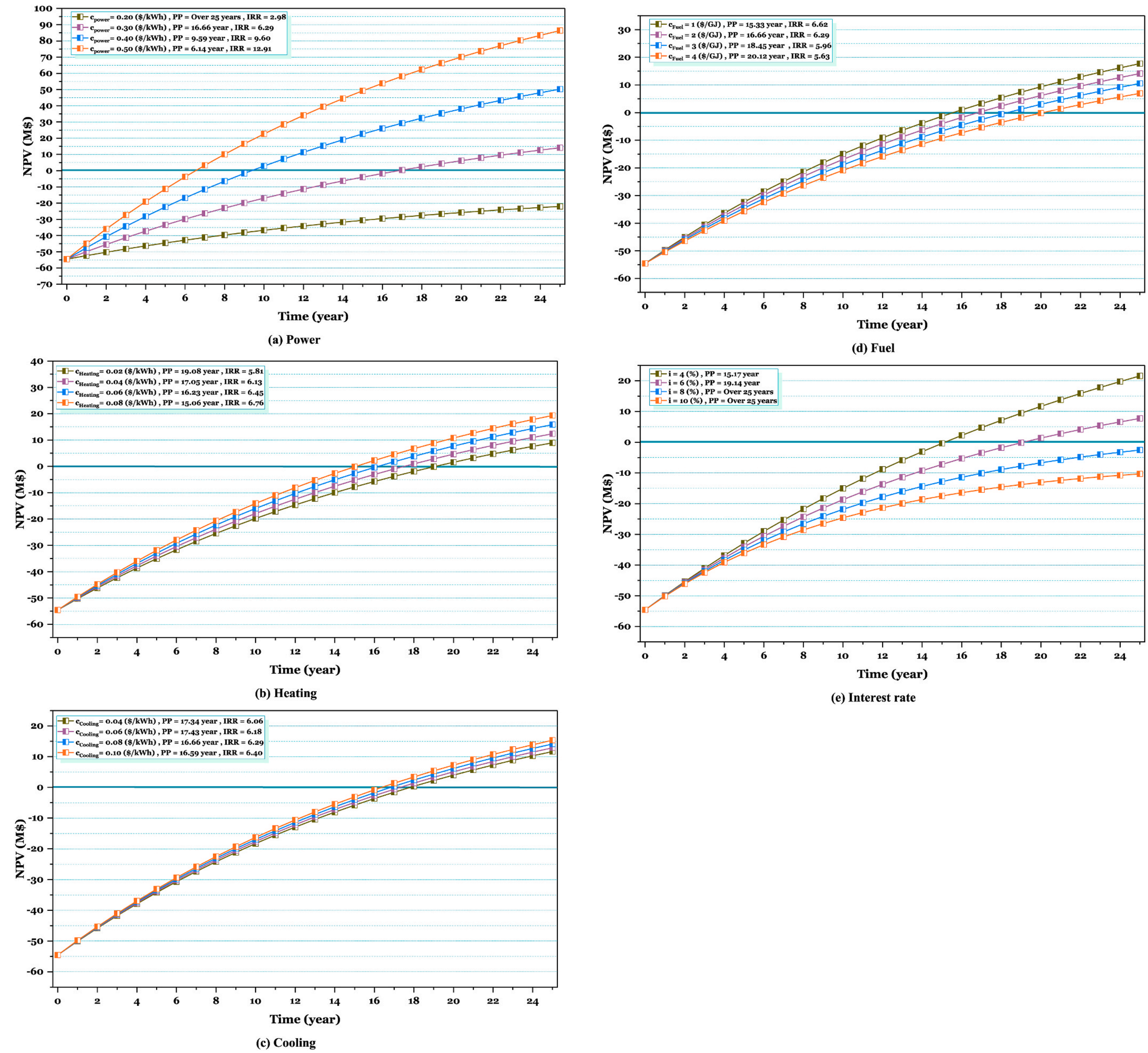

Fig. 9. NPV evaluations of power, heating, cooling, fuel, and interest rate over a 24-year period under varying price scenarios, PP, and IRR values.

$$\eta_{elect} = \frac{\dot{W}_{net}}{\dot{Q}_f} \tag{20}$$

where the net power output is:

$$\dot{W}_{net} = \sum \dot{W}_T - \sum \dot{W}_K - \dot{W}_P \tag{21}$$

Lastly, the following formula is used to determine the proposed CPP's fuel saving potential (FSP) in comparison to a traditional separate production (SP) system (electricity from a turbine, hot water from a boiler, and cooling from an electric chiller) [46]:

$$fuel\ saving\ potential = 1 - \dot{Q}_f^{new} \Big/ \dot{Q}_f^{SP} \tag{22}$$

The required fuel input in the reference SP system is estimated by Ref. [47]:

$$\dot{Q}_f^{SP} = \frac{\dot{W}_{net}}{\eta_{elect}^{SP}} + \frac{\dot{Q}_h}{\eta_{boiler}^{SP}} + \frac{\dot{Q}_c}{\eta_{elect}^{SP} \times COP_{sp}} \tag{23}$$

Here, η_{elect}^{SP}, η_{boiler}^{SP}, and COP_{sp} denote the electrical efficiency, boiler efficiency, and coefficient of performance of the electric chiller, respectively, as reported in Ref. [47].

2.3.2. Thermo-economic performance analysis approach

In order to evaluate the proposed CPP structure's economic viability, the total cost rate ($\dot{C}_{total}$) was used as the main indicator. Three main components are taken into account by this parameter: The cost of biogas fuel ($\dot{C}_{bio}$), the penalty cost associated with carbon dioxide (CO_2) emissions ($\dot{C}_{em}$), as well as the rate of capital investment and maintenance costs for each system component ($\dot{C}_{CI\&M}$). The following is an expression of the governing relationship [48,49]:

Table 10
Comprehensive performance metrics of the proposed CPP setup.

Parameters	Value
Net power out (kW)	3205
Heating power (kW)	1536
Cooling load (kW)	544
Biogas LHV (kJ/kg)	8829
System energy efficiency (%)	59.86
System exergy efficiency (%)	36.51
System electricity efficiency (%)	36.30
Fuel saving potential (%)	25.32
OBC energy efficiency (%)	15.11
CBC energy efficiency (%)	25.06
MKC energy efficiency (%)	21.90
Penalty cost of CO_2 emission ($/h)	368
Total investment and maintenance costs ($)	54552786
Total investment and maintenance costs rate ($/h)	512.90
Fuel cost rate ($/h)	68.52
Total cost rate ($/h)	1017
TPC ($/GJ)	75.89
COE ($/kWh)	0.179
NPV (M$)	14.1136
PP (years)	16.6686
IRR (%)	6.2936
Specific CO_2 emission, SCE (kg/kWh)	0.365
Power emission (kg/kWh)	0.543
Exergo-environmental index (–)	0.634
Environmental damage effective index (–)	1.739
Exergo-environmental impact improvement (–)	0.575
Exergetic stability factor (–)	0.533
Exergetic sustainability index (–)	1.108
GWP_{direct} ($kgCO_{2\text{-}eq}$/h)	1743
$GWP_{indirect}$ ($kgCO_{2\text{-}eq}$/h)	2757
GWP_{total} ($kgCO_{2\text{-}eq}$/h)	4500
GWP per kWh ($kgCO_{2\text{-}eq}$/kWh)	0.051

$$\dot{C}_{total}(\$/h) = \dot{C}_{em} + \dot{C}_{bio} + \sum_{j=1}^{n} \dot{C}_{CI\&M} \tag{24}$$

The individual cost terms are obtained using the following equations [48,50]:

$$\dot{C}_{em} = \dot{m}_{CO_2} \times C_{CO_{2,f}} \tag{25}$$

$$\dot{C}_{bio} = \dot{m}_{CO_2} \times C_{bio,f} \tag{26}$$

$$\dot{C}_{CI\&M} = \frac{1.06 \times Z_j \times CRF}{H} \tag{27}$$

$$CRF = \frac{I_r(1+I_r)^L}{(1+I_r)^L - 1} \tag{28}$$

$$Z_{k,Ref.} = Z_{k,base} \times \frac{CEPCI_{k,Ref.}}{CEPCI_{k,base}} \tag{29}$$

where $C_{CO_{2,f}}$ shows the penalty cost factor of CO_2 emissions, $C_{bio,f}$ the biogas cost factor, H the annual operating hours, Z_j the total investment cost of component j, as well as CRF presents capital recovery factor, I_r the interest rate, and L is the system lifetime.

Moreover, in order to ensure consistency with inflation-adjusted cost indices, the cost-scaling relation in Eq. (29) is frequently used to update capital costs of equipment from published data or vendor quotes in a given base year to a desired reference year. In this equation, $Z_{k,Ref.}$ denotes updated cost of equipment k at the reference year, $Z_{k,base}$ base cost of equipment k at the base year. Plus, chemical engineering plant cost index value for the reference year is depicted by $CEPCI_{k,Ref.}$, and for the base year is denoted by $CEPCI_{k,base}$ [51].

In addition, the values of the key economic parameters used for the analysis are summarized in Table 3. Meanwhile, Table 4 presents the cost functions employed to estimate the investment cost of each major equipment component in the proposed CPP, along with the base year and CEPCI values used for cost scaling.

In addition to cost rate analysis, several economic performance indicators were also evaluated:

$$NPV = -TCI + \sum_{n=0}^{N} Y(1+i)^{-n} \tag{30}$$

$$TCI = \sum Z_j \tag{31}$$

$$Y = AI - \left(C^{O\&M} - \dot{C}_{bio}\right) \tag{32}$$

Here, net present value (*NPV*) assesses the project profitability by discounting cash flows, total capital investment (*TCI*) represents the total cost of purchasing and installing all system equipment, calculated as Eq. (31), Y is the annual net cash flow, given by Eq. (32), N shows the project lifetime in years, i is the discount rate, representing the time value of money, and n year of the project lifetime, ranging from 0 to N. Moreover, in Eq. (32), AI represents annual income from selling electricity, heat, and cooling, and $C^{O\&M}$ operation and maintenance costs [55,62].

Payback period (*PP*) is the amount of time needed for the cumulative net cash flows to be greater than the sum of the net present values (NPV (n) > 0) [55].

$$PP = min\{n : NPV(n) > 0\} \tag{33}$$

Internal rate of return (*IRR*) is the discount rate that makes $NPV = 0$, obtained from Eq. (34), in which net cash flow for year n is depicted by $Cash\ flow_n$ [62,63].

$$0 = NPV = \sum_{n=0}^{N} \frac{Cash\ flow_n}{(1+IRR)^n} \tag{34}$$

COE (cost of energy) is calculated based on Eq. (35), in which $\dot{C}_{total}$ is the overall cost rate of the system, and *En* overall useful energy produced (net electricity, heating, and cooling) [57].

$$COE = \frac{\dot{C}_{total}}{\sum En \times H} \tag{35}$$

Finally, the total product cost ($c_{product}$) can be determined based on Eq. (36), in which the total energy outputs (net power, heating, and cooling) are regarded as [48]:

$$\dot{C}_{total}\ (\$/h) = c_{product}\ (\$/GJ) \times \left(\dot{W}_{net} + \dot{E}_{heat} + \dot{E}_{cooling}\right)\ (GJ/h) \tag{36}$$

2.3.3. Environmental performance analysis approach

There can still be CO_2 emissions from combustion if biogas is used as a renewable energy source. Both net and total emissions are used to evaluate these emissions. While net emissions are calculated by deducting the CO_2 in the fuel from total emissions, total emissions take into consideration both direct and indirect contributions [64].

$$CO_2^{net} = total\ emission - CO_2^{used} \tag{37}$$

To measure the emissions per unit of useful energy produced, the specific CO_2 emission (*SCE*) can be calculated using Eq. (38) after the net CO_2 emission has been determined [65]:

$$\delta_{CO_2} = \frac{net\ emission}{\dot{W}_{net} + \dot{Q}_c + \dot{Q}_h + \dot{E}x_h} \tag{38}$$

Furthermore, the current system's emission reduction (*EMR*) in comparison to traditional systems with comparable output can be calculated as follows:

$$EMR = \left(\delta_{CO_{2,i}} - \delta_{CO_2}\right) \times \sum useful\ energy \tag{39}$$

where $\delta_{CO_{2,i}}$ represents the CO_2 emission intensity of the reference system [65].

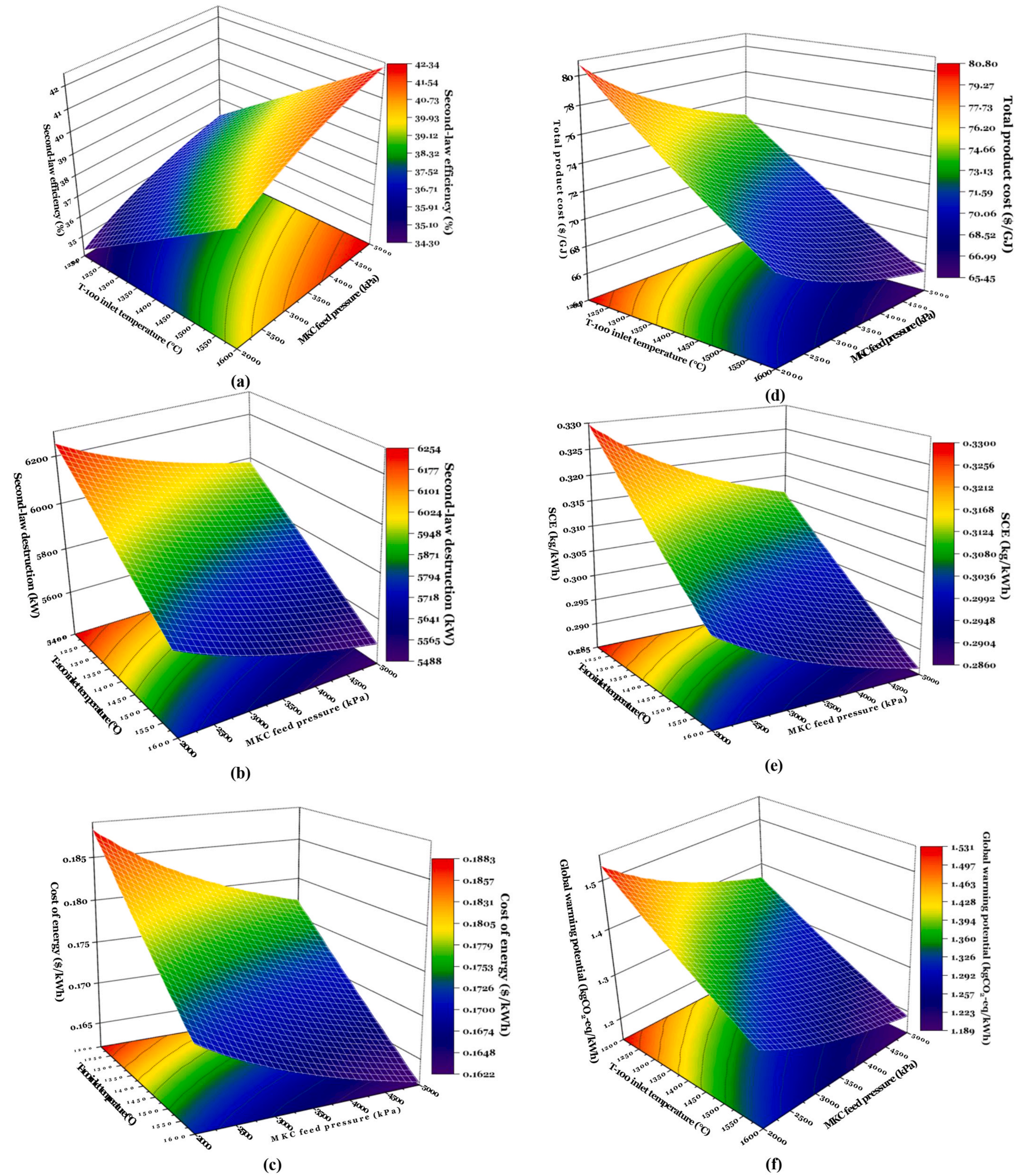

Fig. 10. Effect of MKC feed pressure and T-100 inlet temperature on the major output parameters of the new CPP.

In addition, an LCA (life cycle assessment) was implemented using a well-defined gate-to-gate boundary to quantify the system's global warming potential (*GWP*). This assessment captures both direct and indirect emissions specifically attributed to the internal power conversion processes, thereby providing a focused and reproducible environmental evaluation of the proposed system configuration.

$$Total\ GWP\left(kgCO_{2-eq}\ FU^{-1}\right) = \sum GWP_{direct} + \sum GWP_{indirect} - CapturedCO_2 \tag{40}$$

In the current study, the LCIA (life cycle impact assessment) factor

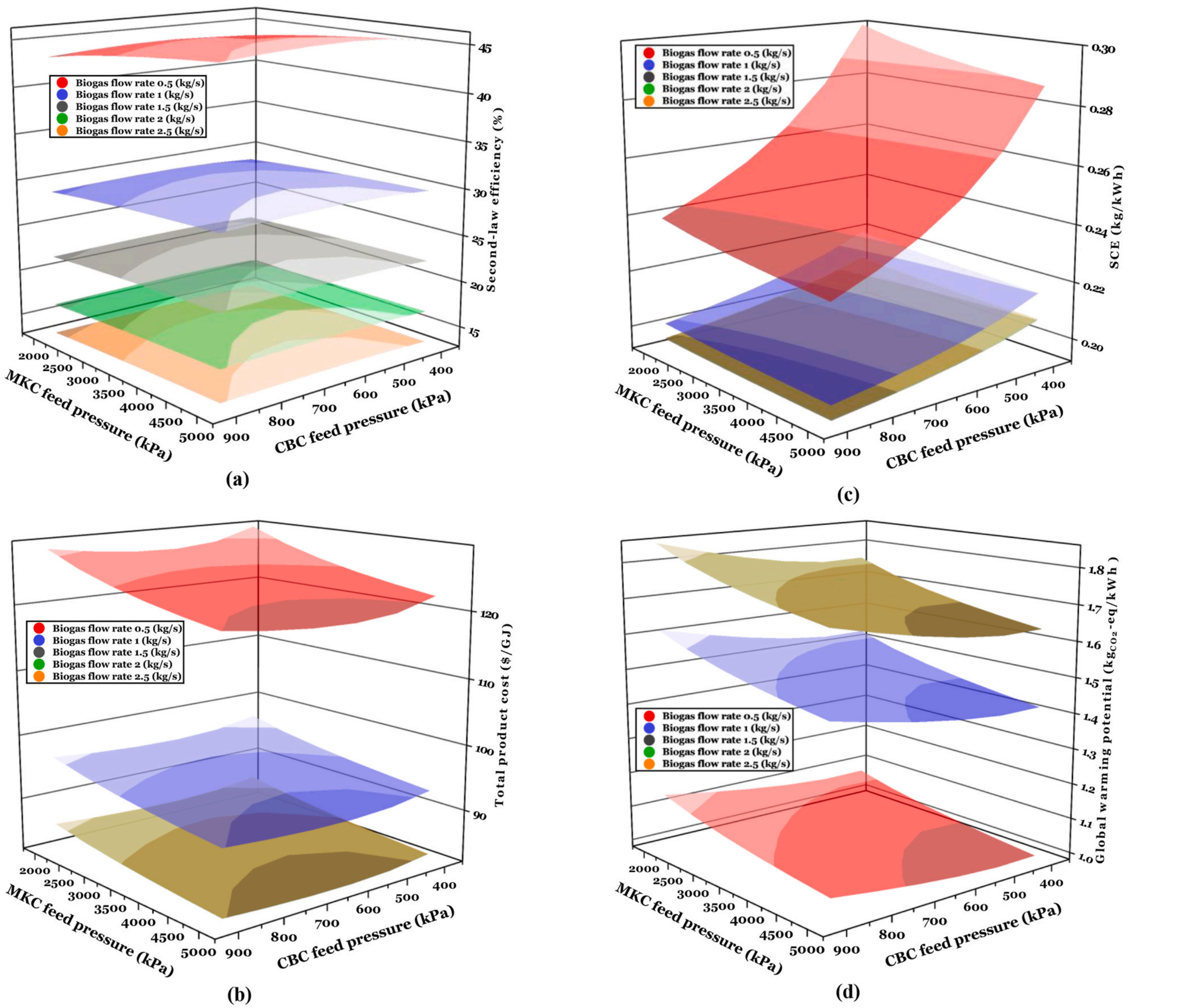

Fig. 11. Effect of CBC and MKC feed pressures, and biogas flow rate on the key output parameters of the new CPP.

for indirect emissions associated with cooling was regarded as 0.61365 kg CO_2-eq/kWh [66].

Also, the exergy-enviro parameters added, which enable a comprehensive understanding of the relationship between exergy destruction and system performance and environmental burden, improved the environmental assessment of the proposed system. The need to use irreversibilities in the system is reflected in the exergo-environmental index (EEI), which is the ratio of total exergy destruction to the inlet (*in*) exergy flow. Greater thermodynamic losses and, thus, a higher environmental load are indicated by a higher EEI [57,67].

$$EEI = \frac{\dot{E}x_{d,total}}{\dot{E}x_{in}} \tag{41}$$

This evaluation is further expanded by the environmental damage effectiveness index (EDEI), which normalizes EEI in relation to exergy efficiency. It reflects the capacity of the system to reduce ecological damage in the use of existing resources and yield beneficial results. A system that achieves a better balance between environmental responsibility and performance is indicated by a lower EDEI value [57,67].

$$EDEI = \frac{EEI}{\varepsilon_{sys}} \tag{42}$$

In addition, a direct indicator of the potential for environmental improvement is offered by the exergo-environmental impact improvement (EII), which is the reciprocal of EDEI. A higher EII indicates a more environmentally friendly and sustainable system configuration [57,67].

$$EII = \frac{1}{EDEI} \tag{43}$$

By assessing the connection between exergy destruction and the production of useful products, the exergetic stability factor (ESF) provides information about how resilient the system is to changing operating circumstances. A stable design that is less vulnerable to environmental inefficiencies is indicated by a high ESF [57,67].

$$ESF = \frac{\dot{E}x_{d,total}}{\dot{E}x_{d,total} + total\ product + 1} \tag{44}$$

Lastly, as a comprehensive sustainability indicator, the exergetic sustainability index (ESI) combines the ESF and EII. Configurations with higher ESI values are those that improve long-term viability, reduce environmental degradation, and guarantee stability all at once [57,67].

$$ESI = ESF \times EII \tag{45}$$

All things considered, these parameters enable a multifaceted

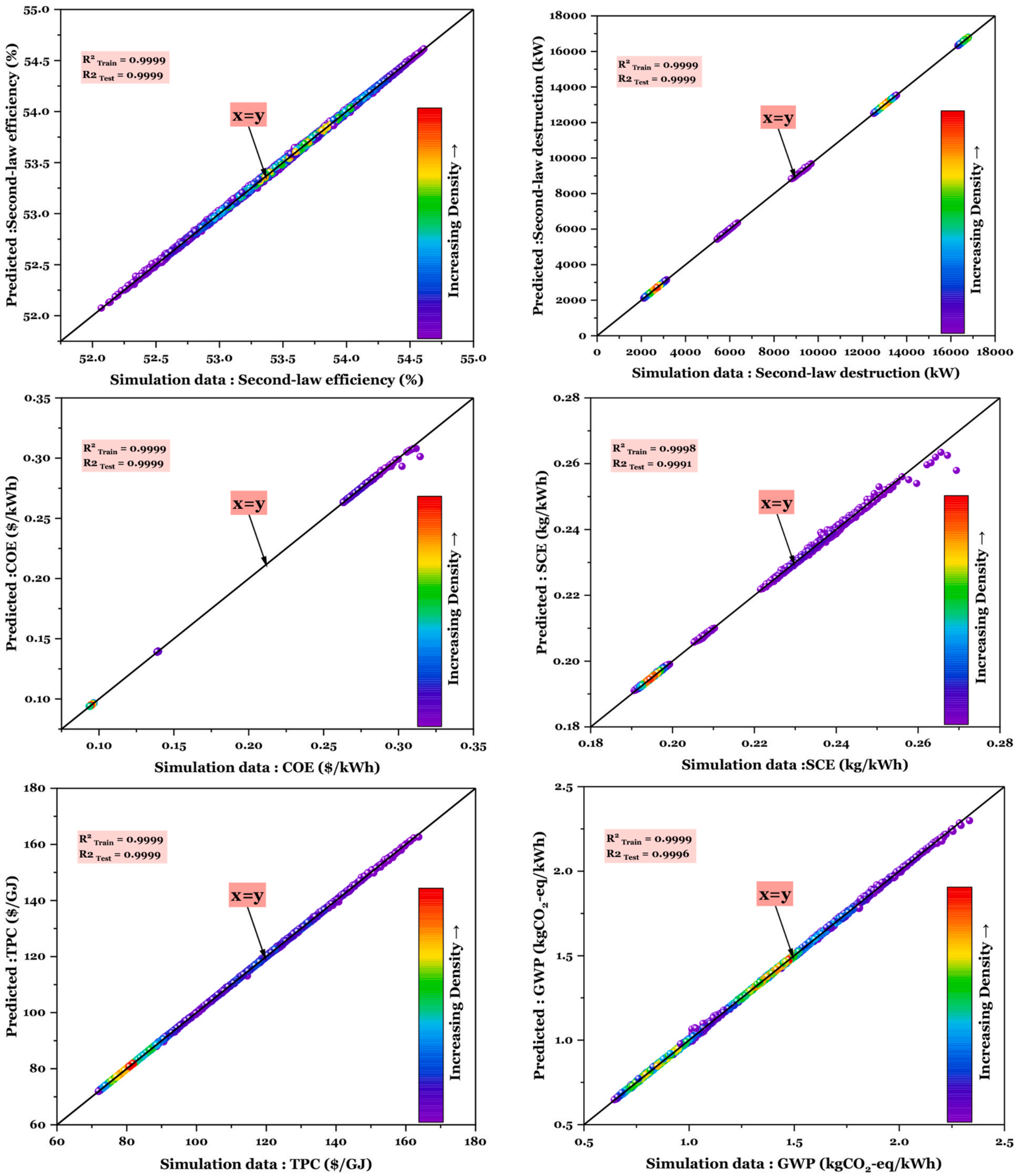

Fig. 12. R^2 plots of ANFIS model predictions versus simulation data for the new system's thermodynamic, economic, and environmental indicators.

environmental evaluation of the suggested CPP setup. They represent a more stringent approach than energy or emission-based indicators, and more than just quantifying the magnitude of environmental impact they also identify stability, long term sustainability and improvement potential.

2.3.4. ML and MOO approaches

To predict key system performance metrics accurately, an ANFIS (Adaptive Neuro-Fuzzy Inference System) was deployed, enhancing operational understanding and facilitating sound decision-making. The combination of fuzzy logic reasoning with neural networks' learning ability makes ANFIS an intelligent hybrid ML model that can capture certain complex nonlinear input-output relationships [68,69]. A set of 3219 steady-state samples was used to train the ANFIS model, with 75% of the training dataset and 25% of the independent hold-out test set for a rigorous evaluation of the ANFIS model. Additionally, to verify the model's generalization capability and confirm the absence of overfitting, a five-fold cross-validation strategy was implemented, with results averaged across all iterations to derive final performance metrics. The architecture and hyperparameter settings, which were fine-tuned through the hybrid optimization method, are detailed in Table 5.

Next, MOO was implemented for the CPP setup under study in order to attain the best possible trade-off between economic performance, environmental impact, and energy efficiency. In order to manage the

Table 11
Evaluated metrics of the ANFIS for test and train datasets, showing excellent prediction accuracy across thermodynamic, economic, and environmental targets.

Target	RMSE	MAE	R^2	MAPE
Train				
Second-low efficiency	0.0008	0.0006	0.9999	0.1925
Second-low destruction	2.5732	1.9678	0.9999	0.0341
COE	0.0001	0.0001	0.9999	0.0395
TPC	0.0829	0.0566	0.9999	0.0542
SCE	0.0003	0.0002	0.9998	0.0718
GWP	0.0035	0.0026	0.9999	0.2142
Test				
Second-low efficiency	0.0012	0.0008	0.9999	0.2783
Second-low destruction	7.9792	4.4571	0.9999	0.0747
COE	0.0007	0.0001	0.9999	0.0541
TPC	0.2240	0.1329	0.9999	0.1198
SCE	0.0006	0.0003	0.9991	0.1099
GWP	0.0073	0.0048	0.9996	0.3910

contradictory character of these objectives, four metaheuristic algorithms, including Grey Wolf Optimizer (GWO), Particle Swarm Optimization (PSO), Artificial Rabbits Optimization (ARO), and NSGA-II, were used and compared. The special exploration and exploitation features offered by each algorithm help one to fully assess the topography of the system's optimization. Using these techniques therefore, the CPP design was evaluated in several scenarios in order to identify Pareto-optimal solutions that balance thermo-enviro-economic performance of the suggested system. Table 6 defines the operational boundaries for the key design parameters utilized in the MOO process, providing the search space for the applied metaheuristic algorithms to identify optimal system configurations.

Fig. 3 illustrates the implementation process of the ARO algorithm. ARO algorithm is a population-based metaheuristic algorithm that is inspired by the foraging and hiding nature of rabbits. It is a method that switches between "exploration" and "exploitation," using a pair of search strategies: *detour foraging* and *random hiding*, and an *energy shrink* mechanism to manage the switching between the phases [70]. In the exploration stage, each rabbit updates its position by moving toward a randomly chosen peer in the swarm and adding a perturbation, which promotes diversified search over the solution space. This *detour foraging* behavior is defined as [70]:

$$\vec{v}_i(t+1) = \vec{x}_j(t) + R\times\left(\vec{x}_i(t)-\vec{x}_j(t)\right) + \text{round}(0.5\times(0.05+r_1)) \times n_1, i,j = 1,\dots,n \text{ and } j\neq i \tag{46}$$

where R shows the running operator:

$$R = L\times c \tag{47}$$

$$L = \left(e - e^{\left(t-1/T\right)^2}\right)\times \sin\left(2\pi r_2\right) \tag{48}$$

The parameter c governs the direction based on a random permutation g of the dimensions d:

$$c(k) = \begin{cases} 1 & \text{if } k == g(l) \\ 0 & \text{else} \end{cases}, k = 1,\dots,d \text{ and } l = 1,\dots,\left\lceil r_3\times d\right\rceil \tag{49}$$

$$g = \text{randperm}(d) \tag{50}$$

$$n_1 \sim N(0,1) \tag{51}$$

In the exploitation stage (*random hiding*), rabbits search for promising solutions by moving toward a randomly selected burrow, which intensifies the search around high-quality regions. That is, for avoiding predators, rabbits hide in one of d randomly selected burrows, intensifying the search:

$$\vec{v}_i(t+1) = \vec{x}_i(t) + R\times\left(r_4\times\vec{b}_{i,r}(t)-\vec{x}_i(t)\right), i = 1,\dots,n \tag{52}$$

The burrow selection is specified by:

$$g_r(k) = \begin{cases} 1 & \text{if } k == \lceil r_5\times d\rceil \\ 0 & \text{else} \end{cases}, k = 1,\dots,d \tag{53}$$

$$\vec{b}_{i,r}(t) = \vec{x}_i(t) + H\times g_r\times\vec{x}_i(t) \tag{54}$$

After either strategy, the position is updated if the new candidate position yields better fitness:

$$\vec{x}_i(t+1) = \begin{cases} \vec{x}_i(t) & f\left(\vec{x}_i(t)\right)\le f\left(\vec{v}_i(t+1)\right) \\ \vec{v}_i(t+1) & f\left(\vec{x}_i(t)\right) > f\left(\vec{v}_i(t+1)\right) \end{cases} \tag{55}$$

To balance exploration and exploitation over the course of iterations, ARO introduces an *energy* factor $A(t)$ defined in Eq. (56), which decreases over time T with iteration number and gradually shifts the algorithm from *detour foraging* toward *random hiding*. This adaptive mechanism enables ARO to explore the search space broadly at the beginning and refine the solutions effectively in later iterations [70].

$$A(t) = 4\left(1-\frac{t}{T}\right)\ln\frac{1}{r} \tag{56}$$

In the above equation $r\in(0,1)$ presents a random number. When $A>1$, the rabbits perform *detour foraging*; otherwise, they perform *random hiding*.

Table 12
MOO scenario results showing improvements in efficiency, economic performance, and environmental impact across different algorithms and scenarios.

Design parameters	Base case	Bi-objective scenario-GWO	Bi-objective scenario-NSGA-II	Bi-objective scenario-PSO	Bi-objective scenario-ARO	Four-objective scenario
$\dot{m}_{biogas}$ (kg/s)	1	1.28	1.02	1.28	1.23	1.12
$T_{in\ T-100}$ (°C)	1200	1558	1575	1588	1567	1580
$P_{CBC\ feed}$ (kPa)	900	928	931	928	906	1066
$P_{MKC\ feed}$ (kPa)	4000	4055	4574	4055	4572	3924
$P_{out\ k-100}$ (kPa)	800	720	751	720	781	757
Performance						
Second-low efficiency (%)	36.51	36.87	37.35	37.87	39.35	38.68
Second-low destruction (kW)	6042	5553	5550	5547	5526	5531
COE ($/kWh)	0.179	0.149	0.145	0.142	0.139	0.138
TPC ($/GJ)	75.89	73.51	71.28	70.51	68.28	68.007
SCE (kg/kWh)	0.315	0.242	0.234	0.214	0.208	0.206
GWP ($kg_{CO2\text{-}eq}$/kWh)	1.404	1.120	1.101	1.019	1.012	1.014

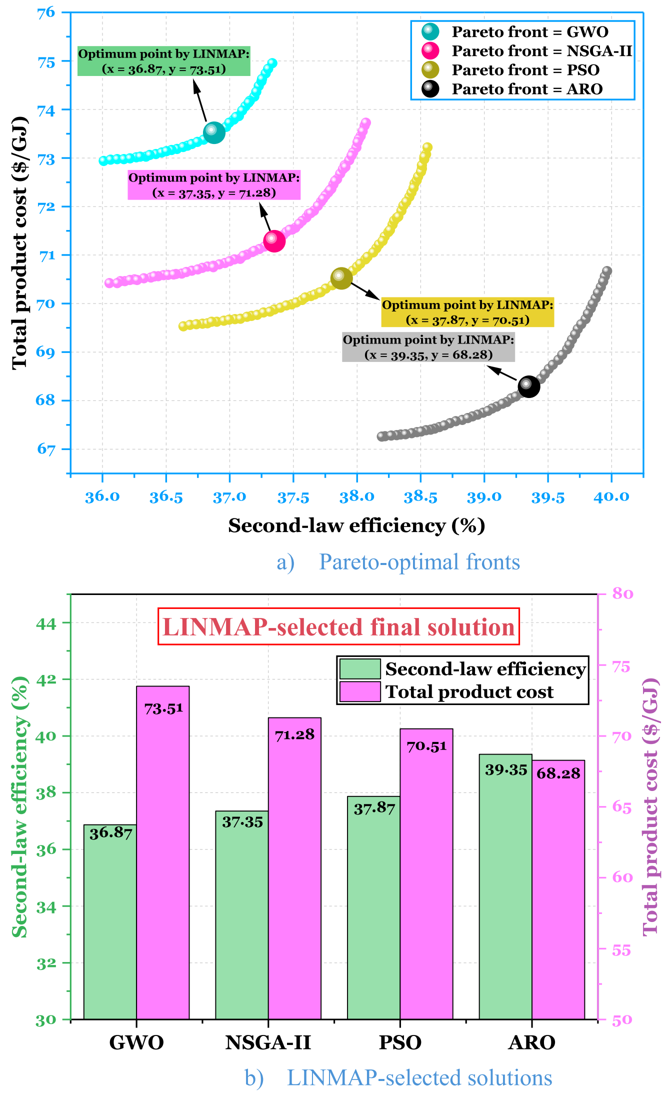

Fig. 13. Comparison of a) Pareto-optimal fronts and b) LINMAP-selected solutions for bi-objective optimization (efficiency–cost trade-off) using GWO, NSGA-II, PSO, and ARO algorithms.

Table 7 provides a summary of the hyperparameter configurations utilized for each metaheuristic algorithm. These parameters were selected based on validated configurations from relevant literature to ensure consistent and equitable performance evaluation across all comparative methods [71–73].

3. Results and discussion

3.1. Verification of the CPP's units

Comparing the studied CPP simulation findings with published data from Refs. [74] and [75], Figs. 4 and 5 validate them. The relative error for each parameter is also reported. The deviation between the reference data and this work is very small as shown, confirming the reliability and accuracy of the adopted simulation approach. Ref. [74] investigated the OBC system fueled by biogas under similar operating conditions, making it a relevant benchmark for comparison. Reference [75], on the other hand, focused on the MKC for electricity generation. The study provided complete input datasets and key performance outputs, which enabled an effective validation of the baseline Kalina modeling in this work.

3.2. Energy-exergy performance analysis results

Under the base design condition, the suggested system provides 544 kW of cooling power, 1536 kW of thermal (heating) power and 3205 kW of net electrical power. The applied cycles MKC, CBC, and OBC have energy efficiencies of 21.9%, 25.06%, and 15.11%, respectively. The overall energy efficiency, overall exergy efficiency, and electrical efficiency of the integrated CPP setup were determined to be 59.86%, 36.51%, and 36.3%, respectively, with a potential for fuel savings of 25.32%, taking into account the total biogas input of 8829 kW.

According to Fig. 6, the biogas intake provides an exergy of 9517 kW, which is combusted with air to supply heat. Of this, 4665 kW is recovered through the flue gases to drive the CBC and boiler subsystems. Furthermore, waste heat recovery in the CBC enables the MKC to utilize 1459 kW of fuel exergy, facilitating simultaneous electricity and cooling production.

The exergetic performance analysis of the suggested CPP setup is also summed up in Table 8. According to this table, the burner (1908 kW, 82.28% efficiency), heat exchangers E−101 (689 kW) E−100 (602 kW), and turbine T-101 (482 kW) are the main sources (roughly 73%) of the CPP system's 5036 kW total exergy destruction. Combustion is further highlighted as the primary source of irreversibility by the compressor blocks (OBC = 2651 kW, CBC = 1469 kW). On the other hand, valves behave almost perfectly with very little loss, while turbines (efficiencies >92%) and compressors (>94%) operate effectively with comparatively slight destruction. Plus, E−107 (59.83%), E−106 (28.85%), and E−102 (24.34%) all exhibit critical inefficiencies, making them top priorities for system enhancement. All things considered, improving the heat recovery and combustion components would greatly lower irreversibilities and improve cycle performance.

Accordingly, because of the burner's combustion process, which alone is responsible for 72% of the OBC's exergy destruction, Fig. 7 shows that the OBC contributes the largest share of irreversibility (2651 kW). This implies that by lowering entropy generation, reducing irreversibilities associated with combustion could largely enhance performance of the system. In contrast, the E−101 heat exchanger in the CBC accounts for 46.9% of the subsystem's energy destruction, making it a crucial part of specific design enhancements. Optimizing this exchanger or modifying upstream equipment could mitigate entropy generation and improve overall system efficiency.

3.3. Thermo-economic performance analysis results

The proposed CPP's thermo-economic analysis shows a total cost rate of 1017 $/h, which is primarily made up of fuel costs (68.52 $/h) and investment and maintenance costs rate (512.9 $/h), plus an additional 368 $/h CO_2 emission penalty. The total product cost (TPC) is 75.89 $/GJ, which is equivalent to 0.1796 $/kWh for cost of energy (COE). From an investment standpoint, the system shows moderate economic viability with a net present value (NPV) of 14.1136 M$, a payback period (PP) of 16.67 years, and an internal rate of return (IRR) of 6.29%. All things considered, these findings show that even though the system offers environmentally friendly and sustainable energy, financial viability requires careful evaluation of investment and operating expenses.

Furthermore, compressors and turbines account for the majority of the investment, according to the cost analysis of the CPP components in Table 9. The largest equipment expenditures are for K-101 (39.36 M$, 418.49 $/h), K-100 (5.67 M$, 60.27 $/h), T-101 (4.31 M$, 45.81 $/h), and T-100 (1.94 M$, 20.58 $/h). After accounting for 2024 prices, the heat exchangers E−103 (1.86 M$, 19.76 $/h) and E−102, E−101, E−105, E−104, E−107, and E−106 contribute less to the overall costs, ranging from 35,749 $ to 1.08 M$. The cost of the burner is moderate (278,051 $, 2.96 $/h). This analysis emphasizes the importance of major mechanical components in both capital investment and operational economic planning, with compressors and turbines in particular serving

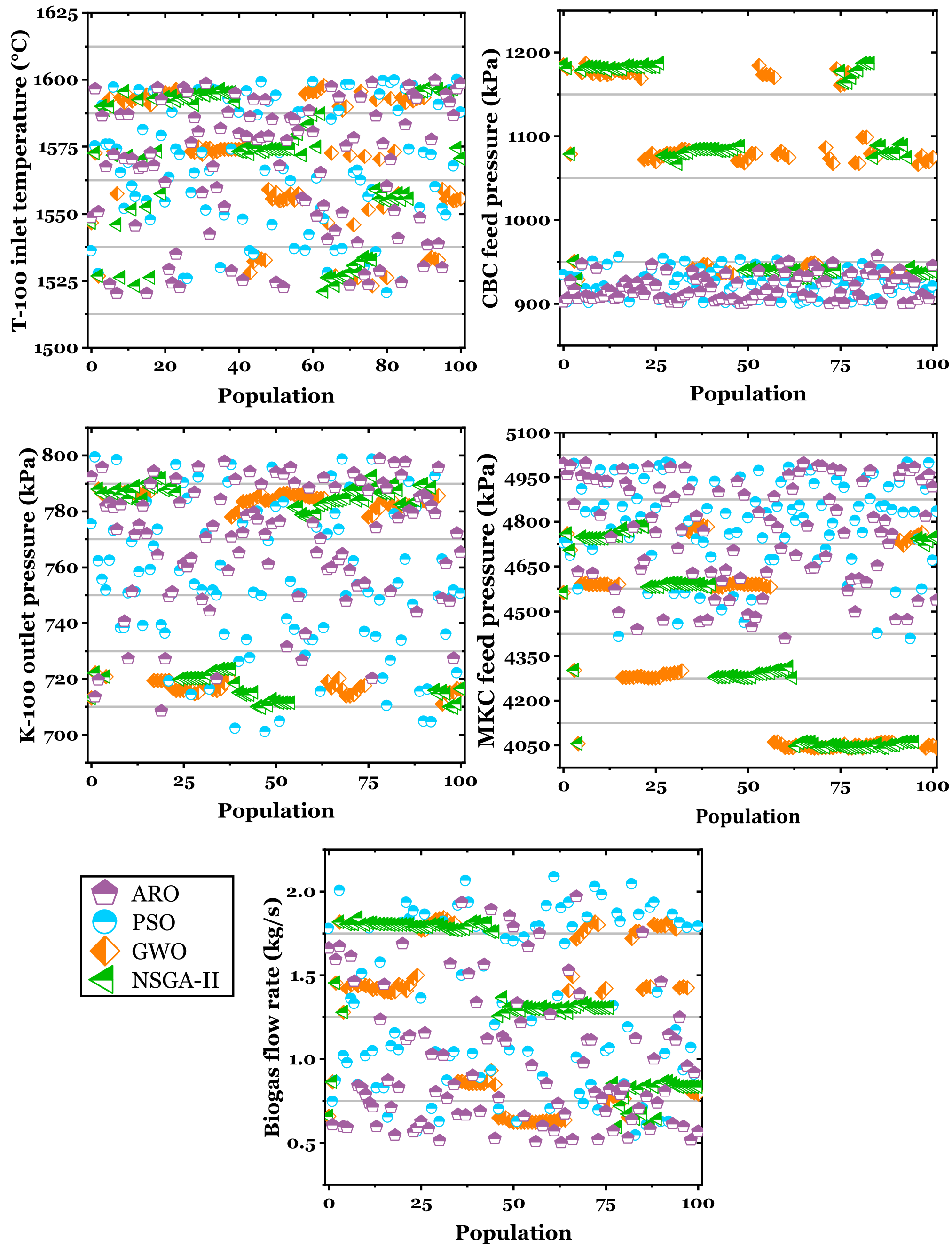

Fig. 14. Scatter plots of decision-variable distributions across populations for the bi-objective optimization algorithms.

as the system's main cost drivers.

In line with this is the outcome of Fig. 8; the figure presents a breakdown of investment costs for various system components, with the largest share allocated to compressors (82.5%), primarily driven by the K-101 component. Expanders (turbines) represent the next significant category at 12.3%, with T-101 contributing the most (64.4%). Smaller parts, such as the burner, coolers and pumps only make up a small fraction of the total investment, highlighting the significance of compressors and expanders.

Fig. 9 presents the plots of NPV assessments for different input-output energy types–power, heating, cooling, and fuel—as well as interest rate over a 24-year period.

The NPV outcomes of the suggested CPP system for a 24-year period at various power prices (0.20 \$/kWh to 0.50 \$/kWh) is displayed in Fig. 9(a). The NPV improves and the project's profitability (IRR) rises as the power price rises. With a payback period of 6.14 years, the power price of 0.50 \$/kWh exhibits the highest NPV and IRR (12.91%). However, with a payback period of more than 25 years, the 0.20 \$/kWh power price scenario has the lowest NPV and IRR (2.98%).

The next plot (Fig. 9(b)) illustrates the NPV over 24 years for four heating price scenarios. The NPV increases with higher heating prices, with the highest price scenario (0.08 \$/kWh) reaching positive NPV around year 15, compared to the lower price scenarios, which remain negative longer. The PP, for the scenarios, ranges from 15.06 years (at heating price of 0.08 \$/kWh) to 19.08 years (at 0.02 \$/kWh), and the IRR increases from 5.81% to 6.76% as the heating price rises.

Next, Fig. 9(c) demonstrates that as the cooling cost increases from 0.04 \$/kWh to 0.10 \$/kWh, the NPV becomes less negative, with the NPV for cooling price of 0.10 \$/kWh reaching closer to zero. Specifically, for cooling price of 0.04 \$/kWh, the NPV exceeds 10 M\$, while

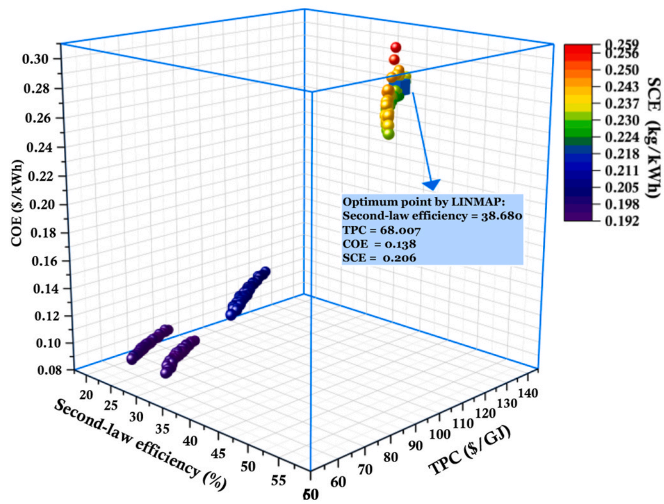

Fig. 15. Four-objective optimization results (via ARO) showing the Pareto distribution of efficiency, cost, and emissions, with the LINMAP-identified optimum point highlighted as the best trade-off solution.

for cooling price of 0.10 $/kWh, it remains around 15 M$. The corresponding PP and IRR values also change: at cooling of 0.04 $/kWh, PP is 17.34 years and IRR is 6.06%, while at cooling of 0.10 $/kWh, PP drops to 16.59 years and IRR increases to 6.40%, suggesting that higher cooling costs slightly improve the project's economic viability.

The NPV plot in Fig. 9(d) shows that the NPV gets more negative as the cost of the fuel input increases, making the project less profitable. The NPV value is around 20 M$ for fuel price of 1 $/GJ and around 5 M$ for fuel price of 4 $/GJ. The PP and IRR also change with increasing fuel cost: at 1 $/GJ, PP is 15.33 years with an IRR of 6.62%, while at 4 $/GJ, PP extends beyond 20 years, and IRR drops to 5.63%. This indicates that the higher the input fuel prices, the worse it is for the payback period and the return on investment.

Finally, Fig. 9(e) presents that as the interest rate increases (i), the NPV becomes more negative, indicating a decline in the project's financial viability. For an interest rate of 4%, the NPV remains around 20 M$, while for 10%, it is −10 M$. The PP also changes: for $i = 4\%$, the PP is 15.17 years, while for $i = 10\%$, the PP extends beyond 25 years. This indicates that the impact of higher interest rates is significant on the economic performance of the project which will result in decrease of the NPV and increase in payback period.

3.4. Environmental performance analysis results

The environmental assessment of the proposed CPP process indicates a net CO_2 emission of 1742 kg/h, considering the CO_2 content in biogas (2489 kg/h) and the total flue gas emissions (4231 kg/h). Plus, based on the process simulation and thermodynamic results, the specific CO_2 emission (SCE) is estimated by 0.3651 kg/kWh, being significantly less than the reference biomass-based system (0.518 kg/kWh) reported in Ref. [65], corresponding to a CO_2 emission reduction of 1075 kg/h.

In addition, exergo-environmental analysis reveals a power emission of 0.5438 kg/kWh, and an exergo-environmental index (EEI) of 0.6349, indicating effective utilization of input fuel with reduced environmental burden. The environmental damage effective index (EDEI) is 1.739, while the exergo-environmental impact improvement (EII), exergetic stability factor (ESF), and exergetic sustainability index (ESI) are 0.5751, 0.5334, and 1.108, respectively, highlighting the system's contribution to sustainable energy production.

On the other side, LCA results show a direct global warming potential (GWP) of 1743 $kgCO_2$-eq/h, an indirect GWP of 2757 $kgCO_2$-eq/h, and a total GWP of 4500 $kgCO_2$-eq/h, corresponding to 0.0514 $kgCO_2$-eq/kWh. The results of these findings show the capability of the proposed system to reduce GHGs emissions and facilitate environmentally friendly power, cooling and heating productions.

Considering the aforementioned results from the system analysis, Table 10 is presented as an overall performance of the proposed CPP, with its energy, exergy and thermo-economic and environmental outputs and efficiencies given for each of the subsystems.

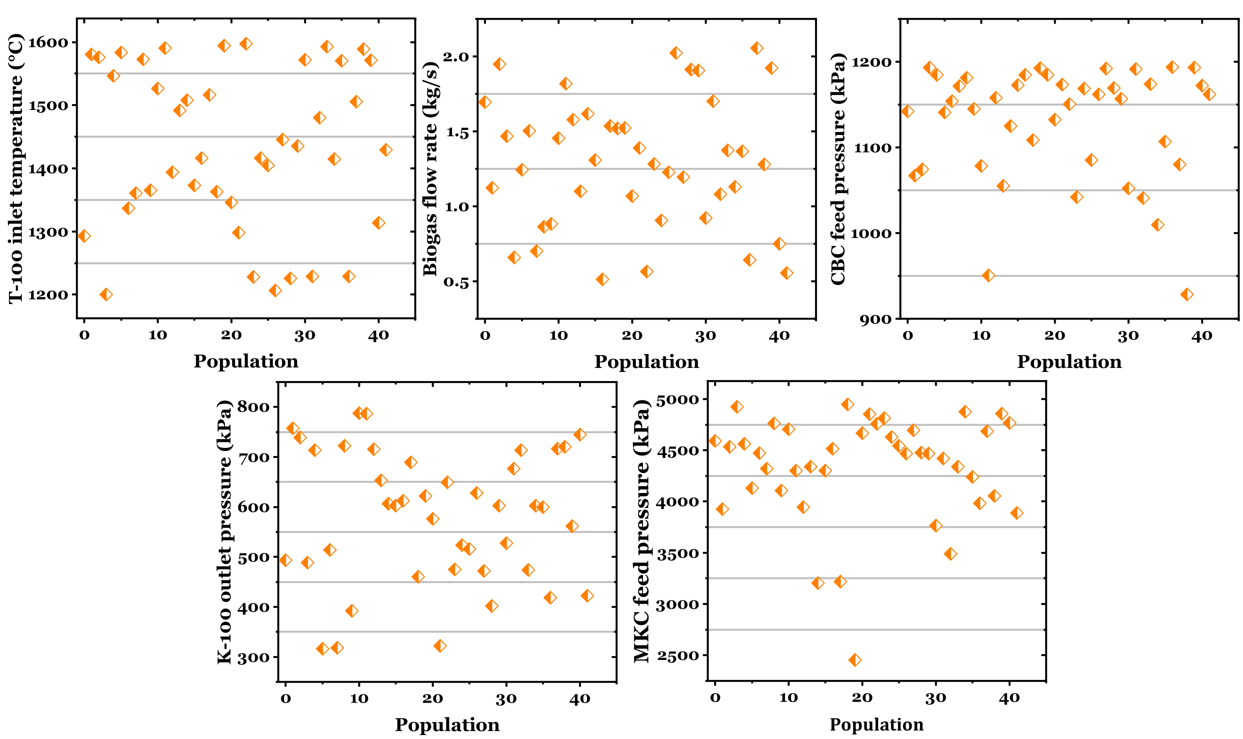

Fig. 16. Scatter plots of decision-variable populations derived from the four-objective optimization.

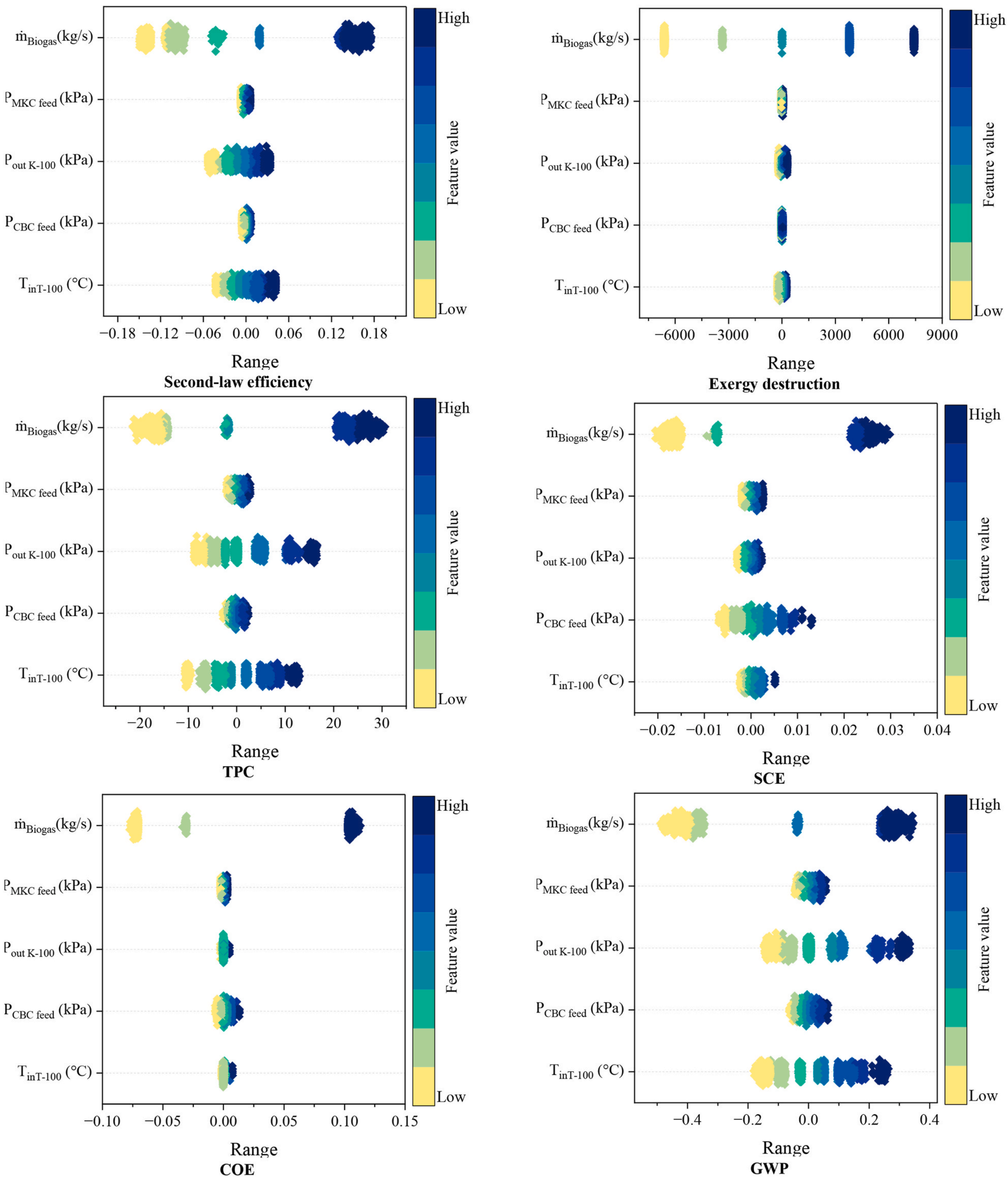

Fig. 17. SHAP-based sensitivity analysis plots showing the relative impact of decision variables on the system performance indicators, highlighting biogas flow rate as the dominant driver across efficiency, environmental, and economic goals.

3.5. Parametric study

The 3D surface plots in Fig. 10 illustrate the impact of two parameters—T-100 inlet temperature (°C) and MKC feed pressure (kPa)—on the suggested CPP system's key output parameters.

Plot (a) shows that higher MKC feed pressures and T-100 inlet temperatures raise second-law efficiency, peaking in the upper right corner of the graph. Precisely as both variables rise, the system's efficiency heads toward 42.34%, the highest value on the graph. The color scale's slope shows that the efficiency is more sensitive to changes in the MKC feed pressure than the T-100 inlet temperature. as shown by the more pronounced surface changes caused by MKC feed pressure rise. The higher values of each of these factors maximize the second-law efficiency of the system and therefore both are very important.

Plot (b) shows how the same input variables affect the second-law destruction of the system. The story shows that as MKC feed pressure and T-100 inlet temperature increase, second-law damage lessens. Second-law damage is at its lowest value, around 5488 kW, in the

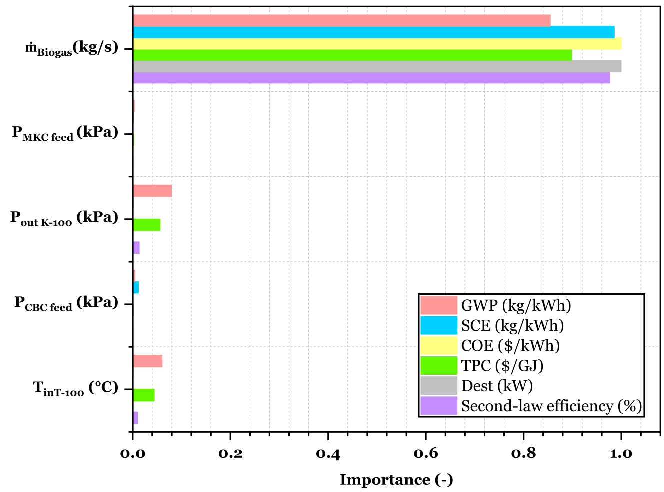

Fig. 18. Feature importance analysis demonstrating biogas flow rate as the most influential variable across all objectives.

bottom right corner of the story when both parameters reach their minimum levels. In contract, at lower MKC feed pressure and T-100 inlet temperature, second-law destruction is maximized, with values nearing 6254 kW. This implies that less entropy generation and system inefficiency result from higher operational parameters, especially T-100 inlet temperature and MKC feed pressure, hence leading to lower second-law damage.

Similarly, apparent for other output factors like COE (plot (c)), TPC (plot (d)), SCE (plot (e)), and GWP (plot (f)) are the same patterns seen for second-law destruction. Increasing T-100 inlet temperature and MKC feed pressure results in better system performance, lower energy losses, financial expenses, and environmental effects in every situation. According to these results, careful optimization of the operating parameters of the major components in the proposed CPP system can simultaneously increase the thermodynamic efficiency, lower the emissions and lower the costs.

The joint effect of CBC and MKC feed pressures as well as biogas flow rate on the proposed CPP system's key output parameters is illustrated in the 3D surface plots of Fig. 11.

Plot (a) represents various biogas flow rates, ranging from 0.5 kg/s to 2.5 kg/s. As the biogas flow rate increases up to 2.5 kg/s, the second-law efficiency decreases, representing the lowest efficiency, around 10%. Additionally, the plot demonstrates that both MKC feed pressure and CBC feed pressure slightly influence efficiency, with higher pressures leading to almost stable performance. Hence, for lower biogas flow rates (e.g., 0.5 kg/s), the second-law efficiency remains higher, around 45%. As the biogas flow rate increases, efficiency values shift toward the lower range (10-15%). This implies that optimizing the performance of the system depends mostly on the biogas flow rate, with reduced rates greatly helping to boost second-law efficiency.

Plot (b) shows that as the biogas flow rate rises to 2.5 kg/s, the TPC declines, signifying the worst economic performance, around 80 $/GJ. Furthermore, the story shows that MKC and CBC feed pressures affect product cost; higher pressures result in almost higher economic performance. Therefore, the price of the product increases (about 130 $/GJ) for lower biogas flow rates (e.g., 0.5 kg/s). The price points move toward the lower range (80-90 $/GJ) as the biogas flow rate grows. This implies that the rate of biogas flow is the most important element in maximizing the economic performance of the system.

Next, Plot (c) shows how the SCE lowers with rising biogas flow rate; the yellow area indicates the smallest emissions near 0.22 kg/kWh. Particularly when the biogas flow rate is greater, the story reveals that higher MKC and CBC feed pressures help to reduce CO_2 emission. As indicated by the red regions of the graph, flow rates (e.g., 0.5 kg/s), the SCE is higher, with values approaching 0.30 kg/kWh. On the other hand, greater biogas flow rates (e.g., 2.5 kg/s) result in emissions as low as 0.22 kg/kWh, the green areas. This indicates that lowering SCE depends critically on both feed pressures and biogas flow rate, thereby emphasizing the need of finding the best values for these. Reduce the environmental effect of the system.

Finally, Plot (d) reveals that as the biogas flow rate rises so does the GWP. The red areas, which represent the lowest biogas flow rate of 0.5 kg/s, show the lowest GWP values—around 1.1 $kgCO_2$-eq/kWh. Conversely, the green regions denoting the greatest biogas flow rate of 2.5 kg/s have the greatest GWP—around 1.9 $kgCO_2$-eq/kWh. The story also shows that greater GWPs are linked to higher CBC feed pressures and that reduced GWPs result from higher MKC feed pressures. This shows that lowering the GWP of the system and helping towards a more environmentally sustainable operation may be accomplished by optimizing biogas flow rates and pressures.

3.6. Results of ML method

Fig. 12 shows the R^2 (determination coefficient) plots comparing the simulation results with the ANFIS model predictions for main thermodynamic, financial, and environmental performance indicators of the suggested CPP system. The results demonstrate that all assessed parameters–second-law efficiency, destruction, COE, TPC, SCE, GWP–attained R^2 values more than 0.999, implying an almost perfect correlation between prediction and simulation. Furthermore, supporting the great precision and generalizing ability of the model across many performance metrics, the tight alignment of all data points along the x = y line verifies this. This demonstrates the reliability of the applied ML approach in capturing the complex thermo-economic and environmental behavior of the system.

In line with this is the results of Table 11 in which the ANFIS model accurately predicts all targets with very high R^2 ($\geq$0.999), minimal relative deviations (MAPE $\leq$0.39), and low errors (RMSE, MAE), confirming its robustness for system performance estimation.

3.7. Results of MOO

A base case with two-objective optimizations employing GWO, NSGA-II, PSO, and ARO is contrasted with a four-objective scenario in Table 12 to display the results of several MOO situations. The outcomes show notable gains over the base case in all optimized cases; i.e. second-law efficiency rises while second-law destruction, COE, TPC, SCE, and GWP fall. For instance, the four-objective scenario maximizes efficiency (38.68%) while minimizing economic costs (COE 0.138 $/kWh, TPC 68 $/GJ), destruction (5531 kW), and environmental effect (SCE 0.206 kg/kWh, GWP 1.014 $kgCO_2$-eq/kWh). Additionally, the efficiency of MOO in directing system design is demonstrated by the fact that, among the two-objective algorithms, ARO regularly offers near-optimal trade-offs, especially in increasing the second-low efficiency, lowering thermodynamic losses, economic, and environmental impacts.

Based on the trade-off between second-law efficiency and TPC, Fig. 13 shows the Pareto-optimal solutions produced by the aforementioned four MOO algorithms. The LINMAP approach was utilized to determine the optimum point in each scenario. As shown in this figure, ARO offers the best compromise, achieving the lowest cost (68.28 $/GJ) and the highest efficiency (39.35%). GWO yields the highest cost (73.51 $/GJ) at relatively low efficiency (36.87%). NSGA-II offers a balanced solution with moderate cost (71.28 $/GJ) and efficiency (37.35%), whereas PSO achieves a slightly lower cost (70.51 $/GJ) with improved efficiency (37.87%). This comparison demonstrates how ARO performs better than the other algorithms by maximizing efficiency and minimizing TPC at the same time.

Fig. 14 presents the population-wise distribution of the main decision variables obtained from the four multi-objective optimization algorithms. The figure shows the inlet temperature (T-100), feed pressure

(CBC), outlet pressure (K-100), feed pressure (MKC), and biogas flow rate. The distribution patterns show clear differences in search behavior among the algorithms. ARO yields comparatively compact solution clusters, indicating stronger convergence and a more focused search around feasible operating regions. PSO, on the other hand, shows a larger variance among the solutions, which indicates less focused search space exploration. GWO and NSGA-II display clustered but more scattered distributions than ARO, suggesting a less uniform convergence behavior. Therefore, the figure indicates that ARO provides a more stable and directed search pattern for the decision variables.

To ensure a rigorous and equitable performance evaluation, it is emphasized that all metaheuristic optimization algorithms (PSO, GWO, NSGA-II, ARO) were conducted using identical decision-variable bounds, as summarized in Table 6. Furthermore, it is important to note that the observed distributions of decision variables—particularly the shifts in parameter ranges—are not artifacts of varying constraints, but rather a reflection of the inherent topography of the Pareto-optimal fronts. In this case, the added conflicting objectives (COE and SCE) caused the optimization framework to be more of a four-objective problem, requiring the search over the entire feasible domain. This leads to the creation of different clusters of populations, which is a reflection of the different strength of the exploration and exploitation abilities of different algorithms in their search of these conflicting search spaces.

Fig. 15 shows a four-objective optimization problem involving second-law efficiency, TPC, COE and SCE. A second-law efficiency of 38.68%, TPC of 68.007 $/GJ, COE of 0.138 $/kWh, and SCE of 0.206 kg/kWh are shown to be the optimal values using LINMAP. This method is a well-balanced compromise that preserves favorable efficiency while lowering costs and environmental effect.

Scatter plots of population distributions for important choice variables derived from the four-objective optimization method are also shown in Fig. 16. T-100 inlet temperature, biogas flow rate, CBC feed pressure, K-100 outlet pressure, and MKC feed pressure are among the parameters. The distribution of points reflects how the optimization is designed to assure diversity in the solution space and explores the ranges of feasible values for each variable. Some parameters, like biogas flow rate and MKC feed pressure, show wider variability, reflecting trade-offs among objectives, while others, like CBC feed pressure and K-100 outlet pressure, show relatively concentrated clusters showing convergence into stable ranges. The relationship between operating conditions and the MOO outcome is highlighted by these scatter distributions.

3.8. Sensitivity analysis

According to the SHAP sensitivity analysis in Fig. 17, biogas flow rate is the primary factor affecting all performance metrics, significantly lowering economic costs (COE and TPC), environmental effect (GWP and SCE), and exergy destruction. Moreover, T-100 intake temperature and K-100 outlet pressure have secondary influence on these metrics, in particular on second-law efficiency, TPC, ASE, and GWP. Generally, the outcomes show that biogas flow is the main variable affecting system behavior, with temperature and operating pressures having complementing but less important effects on trade-offs between efficiency, environment, and cost.

The MOO problem's feature importance analysis is shown in Fig. 18, which also shows how input variables relate to performance metrics including GWP, SCE, COE, TPC, exergy destruction, and second-law efficiency. The results clearly show that biogas flow rate controls and is of greatest importance among all goals, so highlighting its essential part in influencing thermodynamic and economic effects. On the other side, such parameters as T-100 inlet temperature, K-100 outlet pressure, CBC and MKC feed pressures only add tiny contributions and have few impacts on the investigated objectives. This implies that the biogas input primarily determines system performance even if pressure and temperature settings provide fine-tuning corrections rather than causing alterations.

4. Conclusion

To produce electricity, cool, and heat at the same time, a modified Kalina cycle, open and closed air Brayton cycles, and a boiler were coupled in an integrated biogas-fueled combined power plant (CPP). The system was modeled in Aspen HYSYS using energy, exergy, economic and environmental studies. Performance was predicted using machine learning (ANFIS), and optimal operating conditions were identified using multi-objective optimization (MOO) using four metaheuristic algorithms, namely ARO, PSO, GWO, and NSGA-II. Sensitivity analysis measured how design factors affected system behavior.

With 5036 kW of exergy destruction, the CPP achieved overall energy and exergy efficiencies of 59.86% and 36.51%, respectively, producing 3205 kW of electricity, 1536 kW of thermal power, and 544 kW of cooling under base conditions. The total product cost was 75.89 $/GJ and cost of energy equaled 0.1796 $/kWh, with a payback period of 16.67 years and a net present value of 14.1136 M$. Environmentally, CO_2 emissions decreased to 0.365 kg/kWh, and 4500 kgCO_2-eq/h was the total GWP. According to four-objective MOO results, ARO minimized economic and environmental consequences (TPC ≈ 68.007 $/GJ, COE ≈ 0.138 $/kWh, SCE ≈ 0.206 kg/kWh) while maximizing efficiency (≈38.68%). The flow rate of biogas was shown to be the most important element affecting system performance.

These outcomes show the potential of the CPP as a multi-product, sustainable energy source. The study highlights the importance of heat recovery, turbine optimization, and biogas management, providing valuable insights into system design and operation.

4.1. Limitations, practical implementation, and future directions

While the thermo-enviro-economic and optimization results presented herein demonstrate significant potential for the proposed biogas-fired CPP, it is essential to acknowledge the study's reliance on computational modeling and steady-state assumptions. The performance metrics, particularly economic indices such as the payback period and net present value, are subject to real-world fluctuations in feedstock composition, catalyst degradation, and operational wear, which were not captured in this deterministic model. Furthermore, the integration of open and closed Brayton cycles with a modified Kalina cycle significantly increases system complexity, requiring a coordinated control strategy for interdependent variables, such as the turbine inlet temperature, MKC feed pressure, and biogas flow rate. Changes in these parameters, combined with the intermittent nature of biogas production, present challenges for both maintaining stable combustion and thermal recovery efficiency and ensuring thermodynamic stability during transient periods of start-up and shut-down.

To mitigate these operational uncertainties, this study utilizes ANFIS-based predictive modeling to facilitate rapid system assessment, and the ARO algorithm to identify robust operating conditions that maintain efficiency despite fluctuations. However, for commercial scale, advanced real-time monitoring, adaptive control strategies and biogas conditioning units will be required for long term reliability. Finally, future work should consider hardware-in-the-loop (HIL) simulations and pilot scale validation to provide a closer link between the idealized simulation results and actual operation. Additionally, future efforts should prioritize the integration of variable air-excess control strategies to optimize combustion efficiency across the full spectrum of fuel supply fluctuations, alongside exploring integration with secondary renewable sources and dynamic operation modeling.

CRediT authorship contribution statement

Zhao Shuqi: Conceptualization, Investigation. **Yan Limei:** Formal analysis, Methodology. **Mohammad Nadeem Khan:** Data curation, Formal analysis. **Hyder H. Abed Balla:** Investigation, Supervision, Writing – review & editing. **Mohana Alanazi:** Data curation, Validation. **Umid Turdialiyev:** Writing – original draft, Writing – review & editing. **Hind Albalawi:** Funding acquisition, Project administration. **Yasser Fouad:** Conceptualization, Project administration, Resources, Supervision. **Ibrahim Mahariq:** Formal analysis, Investigation, Writing – original draft.

Acknowledgement

Ongoing Research Funding program, (ORF-2026-698), King Saud University, Riyadh, Saudi Arabia. The Provincial Key Research and Development Program of Heilongjiang Province of China under Grant 2024ZXJ01A04.

Appendix A. Supplementary data

Supplementary data to this article can be found online at https://doi.org/10.1016/j.biombioe.2026.109626.

Data availability

The authors do not have permission to share data.

References

[1] A.Q. Al-Shetwi, Sustainable development of renewable energy integrated power sector: trends, environmental impacts, and recent challenges, Sci. Total Environ. 822 (2022) 153645.

[2] W. long Li, Y. Guo, B. Chen, Ming research progress on pyrolysis gasification and resource utilization of tobacco waste: component analysis and recovery strategies, J. Anal. Appl. Pyrolysis 193 (2026) 107425, https://doi.org/10.1016/j.jaap.2025.107425.

[3] V. Pradeshwaran, V. Sundaramoorthy, A. Saravanakumar, A comprehensive review on biogas production from food waste: exploring cutting-edge technologies and innovations, Biomass Bioenergy 188 (2024) 107336.

[4] Z. Yang, N. Yang, Y. Liu, L. Meng, Y. Shen, R. Kuang, Numerical study on self-sustaining isothermal fermentation in a biogas reactor based on thermal flow-reversal reactor, Int. Commun. Heat Mass Tran. 174 (2026) 110934.

[5] S. Ogriseck, Integration of kalina cycle in a combined heat and power plant, a case Study, Appl. Therm. Eng. 29 (2009) 2843–2848.

[6] Y. Feng, Z. Du, M. Shreka, Y. Zhu, S. Zhou, W. Zhang, Thermodynamic analysis and performance optimization of the supercritical carbon dioxide Brayton cycle combined with the kalina cycle for waste heat recovery from a marine low-speed diesel engine, Energy Convers. Manag. 206 (2020) 112483.

[7] M.A. Bagherian, K. Mehranzamir, A comprehensive review on renewable energy integration for combined heat and power production, Energy Convers. Manag. 224 (2020) 113454.

[8] K. Abouemara, M. Shahbaz, G. Mckay, T. Al-Ansari, The review of power generation from integrated biomass gasification and solid oxide fuel cells: current status and future directions, Fuel 360 (2024) 130511.

[9] J. Lu, X. Biogas Gao, Potential, challenges, and perspectives in a changing China, Biomass Bioenergy 150 (2021) 106127.

[10] X. Zuo, Z. Wu, C. Jin, An efficient biogas-assisted Brayton cycle combined with a trigeneration plant with power, heat, water, and methanol outputs: design and multi-criteria analysis, Energy (2025) 137534.

[11] F. Firouzy, M. Yari, V. Zare, F. Ranjbar, A.A.D. Zare, Development and thermodynamic analysis of a biogas-assisted steam methane reforming process combined with a supercritical CO2 Brayton cycle for power, hydrogen, and heat production, Int. J. Hydrogen Energy 140 (2025) 519–531.

[12] A.S. Irani, A. Fattahi, On the combined Brayton-Kalina cycle with PEM hydrogen production: an exergoeconomic analysis and multi-objective optimization with LINMAP decision maker, Int. J. Hydrogen Energy 52 (2024) 289–304.

[13] A.H. Ahmad, M. Aziz, Integration of chemical looping hydrogen generation and ammonia synthesis for power generation at existing natural gas combined cycle, Int. J. Hydrogen Energy (2025).

[14] Z. Shuqi, Y. Limei, V. Goyal, S. Alghanmi, T. Alkhalifah, S. Alkhalaf, F. Alturise, H. E. Ali, A. Deifalla, Artificial neural network-based optimization of baffle geometries for maximized heat transfer efficiency in Microchannel heat sinks, Case Stud. Therm. Eng. 49 (2023) 103331.

[15] A. Wan, Z. Xiong, A.-B. Khalil, R. Yin, J. Yuan, X. Cheng, X. Ji, An integrated TCN-ECA-BiLSTM and TD3 framework for high-accuracy forecasting and optimal load allocation in combined heat and power systems, Energy (2026) 140670.

[16] P. Cheng, X. Jianjun, J. Kumar, H. Almujibah, H.E. Ali, T. Alkhalifah, S. Alkhalaf, F. Alturise, R. Ghandour, Improving efficiency and optimizing heat transfer in a novel tesla valve through multi-layer perceptron models, Case Stud. Therm. Eng. 49 (2023) 103391.

[17] N. Yi, J. Xu, L. Yan, L. Huang, Task optimization and scheduling of distributed cyber–physical System based on improved ant colony algorithm, Future Gener. Comput. Syst. 109 (2020) 134–148.

[18] L.I.U. Limei, X.U. Yongqiang, X.U. Jianjun, X. Aihua, L. Hongyu, G. Jinlan, Broken string diagnosis of composite insulator based on grabcut segmentation and filler area discrimination, Power Syst. Prot. Control 49 (2021) 114–119.

[19] A. Salari, H. Shakibi, A. Habibi, A. Hakkaki-Fard, Optimization of a solar-based PEM methanol/water electrolyzer using machine learning and animal-inspired algorithms, Energy Convers. Manag. 283 (2023) 116876.

[20] K. Jana, S. De, Sustainable polygeneration design and assessment through combined thermodynamic, economic and environmental analysis, Energy 91 (2015) 540–555.

[21] B. Ghorbani, K.B. Mahyari, M. Mehrpooya, M.-H. Hamedi, Introducing a hybrid renewable energy system for production of power and fresh water using parabolic trough solar collectors and LNG cold energy recovery, Renew. Energy 148 (2020) 1227–1243.

[22] M. Abou Houran, M.A. Habila, F. Riaz, M.K. Agrawal, K. Shi, Process development for a novel polygeneration purpose based on tars produced by a biomass gasification unit; Feasibility Study from the thermodynamic, economic, and environmental viewpoints, J. Clean. Prod. 422 (2023) 138636.

[23] J.S. Lopez-Echeverry, S. Reif-Acherman, E. Araujo-Lopez, Peng-robinson equation of state: 40 years through cubics, Fluid Phase Equilib. 447 (2017) 39–71.

[24] D.-Y. Peng, D.B. Robinson, A new two-constant equation of State, Ind. Eng. Chem. Fundam. 15 (1976) 59–64.

[25] Y. Zhang, J. Cruz, S. Zhang, H.H. Lou, T.J. Benson, Process simulation and optimization of methanol production coupled to tri-reforming process, Int. J. Hydrogen Energy 38 (2013) 13617–13630.

[26] R.O. dos Santos, L. de Sousa Santos, D.M. Prata, Simulation and optimization of a methanol synthesis process from different biogas sources, J. Clean. Prod. 186 (2018) 821–830.

[27] S. Saqline, L. Yang, A. Romagnoli, W. Liu, Coupling chemical looping air separation with the Allam Cycle–A thermodynamic analysis, J. Clean. Prod. 418 (2023) 138097.

[28] Z. Liu, J. Shao, H. Guan, X. Jin, H. Zhang, H. Li, W. Su, D. Sun, Optimization of a novel liquid carbon dioxide energy storage System by thermodynamic analysis and use of solar energy and liquefied natural gas, Appl. Therm. Eng. 258 (2025) 124555, https://doi.org/10.1016/j.applthermaleng.2024.124555.

[29] F. Tang, J. Pan, F. Han, J. Yu, J. Fang, R. Li, Sustainable liquid hydrogen production driven by renewable energy, LNG cold energy and industrial waste heat: process design, optimization and comprehensive 4E analysis, Int. J. Hydrogen Energy 205 (2026) 153256, https://doi.org/10.1016/j.ijhydene.2025.153256.

[30] T.U.K. Nutakki, A. Albani, M.K. Agrawal, M.Y. Begum, W. Han, Comprehensive technical Study of a novel polygeneration arrangement using natural gas power plant and geothermal energy for producing electricity, heat, fresh water, and methanol, Process Saf. Environ. Prot. 180 (2023) 98–121.

[31] K.H.M. Al-Hamed, I. Dincer, Investigation of a concentrated solar-geothermal integrated system with a combined ejector-absorption refrigeration cycle for a small community, Int. J. Refrig. 106 (2019) 407–426.

[32] A. Ebrahimi-Moghadam, A.J. Moghadam, M. Farzaneh-Gord, K. Aliakbari, Proposal and assessment of a novel combined heat and power system: energy, exergy, environmental and economic analysis, Energy Convers. Manag. 204 (2020) 112307.

[33] H. Ghaebi, A.S. Namin, H. Rostamzadeh, Performance assessment and optimization of a novel multi-generation System from thermodynamic and thermoeconomic viewpoints, Energy Convers. Manag. 165 (2018) 419–439.

[34] G. Fan, H. Li, Y. Du, S. Zheng, K. Chen, Y. Dai, Preliminary conceptual design and thermo-economic analysis of a combined cooling, heating and power system based on supercritical carbon dioxide cycle, Energy 203 (2020) 117842.

[35] A. Tiktas, H. Gunerhan, A. Hepbasli, Single and Multigeneration rankine cycles with aspects of thermodynamical modeling, energy and exergy analyses and optimization: a key review along with novel System description figures, Energy Convers. Manag. X 14 (2022) 100199.

[36] M.S. Khan, M. Abid, M.A. Bashir, K.P. Amber, S. Khanmohammadi, M. Yan, Thermodynamic and Exergoeconomic Analysis of a Novel Solar-Assisted Multigenerational System Utilizing High Temperature Phase Change Material and Hybrid Nanofluid, 2021.

[37] F. Yilmaz, Performance and environmental impact assessment of a geothermal-assisted combined plant for multi-generation products, Sustain. Energy Technol. Assessments 46 (2021) 101291.

[38] M. Saadat-Targhi, S. Khanmohammadi, Energy and exergy analysis and multi-criteria optimization of an integrated city gate station with organic rankine flash cycle and thermoelectric generator, Appl. Therm. Eng. 149 (2019) 312–324.

[39] B. Ghorbani, M.-H. Hamedi, M. Amidpour, Exergoeconomic evaluation of an integrated nitrogen rejection unit with LNG and NGL Co-Production processes based on the MFC and absorbtion refrigeration systems, Gas Processing Journal 4 (2016) 1–28.

[40] Q. Chen, W. Han, J. Zheng, J. Sui, H. Jin, The exergy and energy level analysis of a combined cooling, heating and power System driven by a small Scale gas turbine at off design condition, Appl. Therm. Eng. 66 (2014) 590–602.

[41] T. Pang, L. Gao, W. Wu, F. Chi, Eco-friendly multi-heat recovery applied to an innovative integration of flue gas-driven multigeneration process and geothermal power plant: feasibility characterization from thermo-economic-environmental aspect, J. Clean. Prod. 449 (2024) 141750.

[42] M. Feili, H. Ghaebi, M.A. Haghghi, Data-Driven optimization of an innovative environmentally friendly power-methanol Co-Production system utilizing biogas-

driven S-Graz cycle, biogas steam reforming, and CO2 capture-hydrogenation process, Renew. Energy 255 (2025) 123835.
[43] G. Liao, F. Zhang, J. Chen, E. Leng, Advanced exergy analysis for organic rankine cycle-based layout to recover waste heat of flue gas, Appl. Energy 266 (2020).
[44] J. Szargut, D.R. Morris, F.R. Steward, Exergy analysis of thermal, chemical, Metallurgical Processes (1987).
[45] S.E. Hosseini, H. Barzegaravval, M.A. Wahid, A. Ganjehkaviri, M.M. Sies, Thermodynamic assessment of integrated biogas-based micro-power generation System, Energy Convers. Manag. 128 (2016) 104–119.
[46] G. Chicco, P. Mancarella, Trigeneration primary energy saving evaluation for energy planning and policy development, Energy Policy 35 (2007) 6132–6144.
[47] R. Jiang, W. Han, F.G.F. Qin, J. Sui, H. Yin, M. Yang, Y. Xu, Thermodynamic model development, experimental validation and performance analysis of a MW CCHP system integrated with dehumidification System, Energy Convers. Manag. 158 (2018) 176–185.
[48] Z. Ghaffarpour, M. Mahmoudi, A.H. Mosaffa, L.G. Farshi, Thermoeconomic assessment of a novel integrated biomass based power generation system including gas turbine cycle, solid oxide fuel cell and rankine cycle, Energy Convers. Manag. 161 (2018) 1–12.
[49] A.H. Mosaffa, L.G. Farshi, C.A.I. Ferreira, M.A. Rosen, Exergoeconomic and environmental analyses of CO2/NH3 Cascade refrigeration systems equipped with different types of flash tank intercoolers, Energy Convers. Manag. 117 (2016) 442–453.
[50] A. Mahmoudan, P. Samadof, S. Hosseinzadeh, D.A. Garcia, A multigeneration Cascade system using ground-source energy with cold recovery: 3E analyses and multi-objective optimization, Energy 233 (2021) 121185.
[51] W. Zhu, J. Han, Y. Ge, J. Yang, W. Liang, Multi-criteria optimization of a combined power and freshwater system using modified NSGA-II and AHP-Entropy-Topsis, Renew. Energy 227 (2024) 120492.
[52] B.-J. Shin, J.-H. Mun, S. Devkota, S.-M. Kim, T.-H. Kang, S.A. Mazari, K. Cho, S. H. Kim, D.-H. Chun, K.-M. Kim, Comparative assessment and multi-objective optimization for the gray and blue ammonia synthesis processes: energy, economic and environmental (3E) analysis, Int. J. Hydrogen Energy 48 (2023) 35123–35138.
[53] S. Devkota, J.-Y. Cha, B.-J. Shin, J.-H. Mun, H.C. Yoon, S.A. Mazari, J.-H. Moon, Techno-economic and environmental assessment of hydrogen production through Ammonia decomposition, Appl. Energy 358 (2024) 122605.
[54] B. Eisavi, F. Ranjbar, H. Nami, Evaluating the techno-economic viability of biomass for green methanol and low-carbon power production, Int. J. Hydrogen Energy 109 (2025) 397–411.
[55] A. Shokri, H. Shakibi, S. Azizi, M. Yari, S.M.S. Mahmoudi, Optimization of biomass-fueled multigeneration System using SOFC for electricity, hydrogen, and freshwater production, Int. J. Hydrogen Energy 88 (2024) 1293–1320.
[56] J. Du, Y. Zou, A. Dahlak, Process development and multi-criteria optimization of a biomass gasification unit combined with a novel CCHP model using helium gas turbine, Kalina cycles, and dual-loop organic flash cycle, Energy 291 (2024) 130319.
[57] S. Ata, Comprehensive evaluation of a gas turbine-based multi-generation System for power, heating, cooling, freshwater, hydrogen and ammonia: 4E assessment and multi-objective optimization with RSM desirability approach, Renew. Energy 246 (2025) 122900.
[58] F. Zhou, W. Cui, L. Yang, Y. Hong, Q. Qian, Simulation and multi-aspect analysis of a novel waste heat recovery process for a power plant producing electricity, heating, desalinated water, liquefied carbon dioxide, and natural gas, Sep. Purif. Technol. 322 (2023) 124244.
[59] J.L. Silveira, C.E. Tuna, Thermoeconomic analysis method for optimization of combined heat and power systems. Part I, Prog. Energy Combust. Sci. 29 (2003) 479–485.
[60] Y. Cao, H.N. Rad, D.H. Jamali, N. Hashemian, A. Ghasemi, A novel multi-objective spiral optimization Algorithm for an innovative Solar/Biomass-Based multi-generation energy System: 3E analyses, and optimization algorithms comparison, Energy Convers. Manag. 219 (2020) 112961.
[61] Z. Xu, Y.-J. Hu, Y.-T. He, T.U.K. Nutakki, A.H. Seikh, V. Mohanavel, N.A. Shah, M. Qin, Thermo-Enviro-economic analysis of a novel landfill gas-fueled CCHP-Desalination process combined with a liquefied natural gas cold energy recovery unit, J. Clean. Prod. 449 (2024) 141675.
[62] S. Devkota, P. Karmacharya, S. Maharjan, D. Khatiwada, B. Uprety, Decarbonizing urea: techno-Economic and environmental analysis of a model hydroelectricity and carbon capture based green urea production, Appl. Energy 372 (2024) 123789.
[63] L. Zhao, Q. Hai, J. Mei, An integrated approach to green power, cooling, and freshwater production from geothermal and solar energy sources; case study of Jiangsu, China, Energy 305 (2024) 132304.
[64] T.B.H. Nguyen, E. Zondervan, Methanol production from captured CO2 using hydrogenation and reforming technologies_ environmental and economic evaluation, J. CO2 Util. 34 (2019) 1–11.
[65] P. Ahmadi, I. Dincer, M.A. Rosen, Development and assessment of an integrated biomass-based multi-generation energy System, Energy 56 (2013) 155–166.
[66] S.-J. Jo, T.-H. Kang, B.-J. Shin, J.-H. Mun, S. Devkota, J.-Y. Cha, S.A. Mazari, K.-M. Kim, U. Lee, C.-H. Shin, Internal carbon loop strategy for methanol production from natural gas: Multi-objective optimization and process evaluation, J. Clean. Prod. 418 (2023) 138140.
[67] M. Shamoushaki, M. Aliehyaei, M.A. Rosen, Energy, exergy, exergoeconomic and exergoenvironmental impact analyses and optimization of various geothermal power cycle configurations, Entropy 23 (2021) 1483.
[68] M. Sedighkia, M. Jahanshahloo, B. Datta, Hybrid neuro fuzzy inference systems for simulating catchment sediment yield, Int. J. Sediment Res. 39 (2024) 305–316.
[69] X. Jianjun, H. Lida, Y. Limei, Y. Na, Insulator self-explosion defect detection based on hierarchical multi-task deep learning, Trans. China Electrotech. Soc. 36 (2021) 1407–1415.
[70] L. Wang, Q. Cao, Z. Zhang, S. Mirjalili, W. Zhao, Artificial rabbits optimization: a new bio-inspired meta-heuristic Algorithm for solving engineering optimization problems, Eng. Appl. Artif. Intell. 114 (2022) 105082.
[71] S. Mirjalili, S. Saremi, S.M. Mirjalili, L. Coelho, S. dos, Multi-Objective grey Wolf optimizer: a novel algorithm for multi-criterion optimization, Expert Syst. Appl. 47 (2016) 106–119.
[72] M.A. Haghghi, M. Feili, P. Nourani, A.M. Bahman, An intelligent NSGA-II-Based optimization of a novel biogas-fed oxyfuel gas turbine cycle using CO2 capture option coupled with a multi-heat recovery network and a multi-effect desalination cycle, Desalination 612 (2025) 118957.
[73] O. Abedinia, H. Shakibi, A. Shokri, B. Sobhani, B. Sobhani, M. Yari, M. Bagheri, Optimization of a syngas-fueled SOFC-Based Multigeneration System: enhanced performance with biomass and gasification agent selection, Renew. Sustain. Energy Rev. 199 (2024) 114460.
[74] M. Yari, S.M.S. Mahmoudi, Utilization of waste heat from GT-MHR for power generation in organic rankine cycles, Appl. Therm. Eng. 30 (2010) 366–375.
[75] H. Rostamzadeh, S.G. Gargari, A.S. Namin, H. Ghaebi, A novel multigeneration System driven by a hybrid biogas-geothermal heat source, part I: thermodynamic modeling, Energy Convers. Manag. 177 (2018) 535–562.